



**HAL**  
open science

## Element distribution in the root zone of ultramafic-hosted black smoker-like systems: Constraints from an Alpine analog

Rémi Coltat, Philippe Boulvais, T. Riegler, E. Pelleter, Yannick Branquet

### ► To cite this version:

Rémi Coltat, Philippe Boulvais, T. Riegler, E. Pelleter, Yannick Branquet. Element distribution in the root zone of ultramafic-hosted black smoker-like systems: Constraints from an Alpine analog. *Chemical Geology*, 2021, 559, pp.119916. 10.1016/j.chemgeo.2020.119916 . insu-02962200

**HAL Id: insu-02962200**

**<https://insu.hal.science/insu-02962200>**

Submitted on 9 Oct 2020

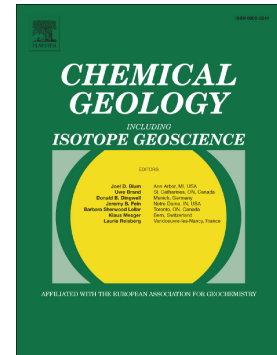
**HAL** is a multi-disciplinary open access archive for the deposit and dissemination of scientific research documents, whether they are published or not. The documents may come from teaching and research institutions in France or abroad, or from public or private research centers.

L'archive ouverte pluridisciplinaire **HAL**, est destinée au dépôt et à la diffusion de documents scientifiques de niveau recherche, publiés ou non, émanant des établissements d'enseignement et de recherche français ou étrangers, des laboratoires publics ou privés.

## Journal Pre-proof

Element distribution in the root zone of ultramafic-hosted black smoker-like systems: Constraints from an Alpine analog

R. Coltat, P. Boulvais, T. Riegler, E. Pelleter, Y. Branquet



PII: S0009-2541(20)30455-1

DOI: <https://doi.org/10.1016/j.chemgeo.2020.119916>

Reference: CHEMGE 119916

To appear in: *Chemical Geology*

Received date: 15 April 2020

Revised date: 15 September 2020

Accepted date: 5 October 2020

Please cite this article as: R. Coltat, P. Boulvais, T. Riegler, et al., Element distribution in the root zone of ultramafic-hosted black smoker-like systems: Constraints from an Alpine analog, *Chemical Geology* (2020), <https://doi.org/10.1016/j.chemgeo.2020.119916>

This is a PDF file of an article that has undergone enhancements after acceptance, such as the addition of a cover page and metadata, and formatting for readability, but it is not yet the definitive version of record. This version will undergo additional copyediting, typesetting and review before it is published in its final form, but we are providing this version to give early visibility of the article. Please note that, during the production process, errors may be discovered which could affect the content, and all legal disclaimers that apply to the journal pertain.

© 2020 Published by Elsevier.

# Element distribution in the root zone of ultramafic-hosted black smoker-like systems: constraints from an Alpine analog

R. Coltat<sup>1</sup>, P. Boulvais<sup>1</sup>, T. Riegler<sup>2</sup>, E. Pelleter<sup>3</sup> and Y. Branquet<sup>1,4</sup>

<sup>1</sup>Géosciences Rennes, CNRS UMR 6118, Université Rennes, F-35000 Rennes, France

<sup>2</sup>Department of Geology, Trinity College Dublin, Dublin, Ireland

<sup>3</sup>IFREMER Centre de Brest, DRO/GM, Plouzané, France

<sup>4</sup>ISTO, UMR7327, Université d'Orléans, CNRS, BRGM, 45071 Orléans, France

Corresponding author: remi.coltat@univ-rennes1.fr

**Keywords:** Ultramafic-hosted black smokers, root zones, element distribution, Mid-oceanic Ridges, extensional detachment, Alps

## Abstract

Fluid-rock interactions at Mid-Oceanic Ridges lead to metal deposition in the so-called seafloor massive sulfides at ultramafic-hosted systems. Due to restricted access to the seafloor and scarcity of 3D exposures, these systems are poorly understood at-depth. A way to access the vertical dimension is to focus on fossil analogs preserved on-land such as the one preserved in serpentinites from the Platta nappe (SE Switzerland). For this example, we document the element distribution in the mineralized rocks at three distinct levels in the rock column using both whole rock chemical analyses and LA-ICPMS analysis of sulfide (chalcopyrite and pyrrhotite) and magnetite. We bring, for the first time, chemical signatures of the mineralization in the root zone of ultramafic-hosted black smokers. At any given depth, the Co/Ni ratio is maximum in the most mineralized samples indicating that this ratio is linked to the intensity of hydrothermal alteration. Additionally, the Co/Ni ratio decreases in mineralized rocks towards the paleosurface, whereas the Se content increases. An episode of carbonation recorded in the highest structural level of the system was responsible for a slight remobilization of the former Cu stock. We propose a model in which the uprising mineralizing fluid mixed with seawater within the host serpentinites, before venting at the paleoseafloor.

## 1. Introduction

Mineralized systems have been recognized and studied in many tectonic settings. At spreading centers, the evidence of active hydrothermalism leading to metal deposition is recorded through the formation of the so-called high-temperature (HT; i.e.  $> 300^{\circ}\text{C}$ ) black and “low-temperature” (LT; i.e.  $250\text{-}300^{\circ}\text{C}$ ) white smokers (Hannington et al., 1995; Tivey, 2007). Over the last three decades, the number of mineralized systems reported along mid-oceanic ridges has considerably increased reinforcing the statement that hydrothermalism is a fundamental process at all spreading-rate mid-oceanic ridges (Beaulieu et al., 2013).

HT black smokers have been firstly recognized along the fast-spreading East Pacific Rise (EPR) in early 80's (RISE Project Group, 1980). The more recent exploration of the slow-spreading Mid-Atlantic Ridge and ultraslow-spreading South West Indian Ridge allowed to identify HT black smoker venting at lower spreading-rate ridges (Rona, 1985; Fouquet et al., 2010; Tao et al., 2012). In these settings, black smokers can be either associated with sedimentary rocks (Zierenberg et al., 1993), mafic rocks (Hannington et al., 1995) or ultramafic rocks where mantle exhumation is accommodated by detachment faulting (i.e. along the oceanic core complexes at slow-spreading ridges, Fouquet et al., 2010).

Because of the nature of the host rock, mineralization at mafic-hosted and ultramafic-hosted hydrothermal systems are slightly different. They consist of Fe-Cu-Zn-rich deposits in mafic settings and Cu-Co-Zn-(Ni)-(Au)-rich deposits in ultramafic settings (e.g. Fouquet et al., 2010). Along the Mid-Atlantic Ridge, these systems were extensively studied through mineralogical (Hannington et al., 1995; Marques et al., 2006), geochemical (Charlou et al., 2002; Rouxel et al., 2004a) or tectonic approaches (McCaig et al., 2007). However, due to restricted access to the seafloor on which the vertical dimension is rarely accessible, ultramafic-hosted mineralized systems have been mainly studied in two dimensions preventing recognition of elemental distribution below the venting site. Hence, this inhibits the complete understanding of the hydrothermal processes forming these systems.

Fossil mineralized systems outcropping on-land represent good opportunities to decipher these processes. Ultramafic-hosted systems have been recognized worldwide in the Bou Azzer ophiolite in Morocco (Leblanc and Billaud, 1982), in Cyprus (Foose et al., 1985; Talhammer et al., 1986), in the Northwestern American Cordillera (Foose, 1985; Candela et al., 1989), in the Eimeshan igneous province in China (Song et al., 2003), in the Outukumpu thrust belt in Finland (Peltonen et al., 2008), in the Urals (Nimis et al., 2008; Maslennikov et al., 2017) and in the Platta nappe (Dietrich, 1972; Coltat et al., 2019b). However, for the most part, the primary extensional structures have been disturbed during subsequent deformation

and metamorphism and the metallic stock has been locally partially reworked. In some cases, the origin of the mineralization is hard to retrieve (Foose, 1985; Talhammer et al., 1896; Song et al., 2003).

In the Platta nappe, Coltat et al., (2019b) recognized a fossil Jurassic ultramafic-hosted black smoker-like system. The overall geometry of this Marmorera-Cotschen hydrothermal system (MCHS) has been preserved from the Alpine overprint. Also, the structural relationships between mineralization, mafic intrusions and detachment fault can be restored. We propose here, based on this geometry, to evaluate the elemental distribution at different structural positions, i.e. at distinct paleo-depths below the detachment, through in-situ LA-ICPMS on metal-bearing phases (chalcopyrite, pyrrhotite, magnetite) and whole rock geochemistry. The geochemical signatures of the MCHS are compared with the ones reported at present-day seafloor massive sulfides (SMS) to better decipher the processes that occur during the ascent of hydrothermal fluids. On this basis, we propose that the mineralizing fluids mixed with seawater within the host serpentinites on their way up to the seafloor.

## 2. Geological setting

The Platta nappe is located in the southeastern part of the Swiss Alps (Grisons' canton) and belongs to the South Pennine Alpine units (figure 1A, B). It represents an ophiolite formed during the opening of the Alpine Tethys basin during the Jurassic. During this period, E-W mantle exhumation was accommodated along detachments faults (figure 1C, Froitzheim and Manatschal, 1996; Epin et al., 2019) and accompanied by mafic magmatism (Desmurs et al., 2002; Amann et al., 2020). U-Pb dating on zircon grains in gabbroic bodies from the Platta nappe yielded an age of  $161 \pm 1$  Ma (Schaltegger et al., 2002). As the magmatic budget in the Platta nappe was low, serpentinitized mantle rocks commonly crop out at the surface where they are covered by mafic extrusives or post-rift sediments (figure 1B, Dietrich, 1970; Epin et al., 2019). As such, the Platta nappe corresponds to an "amagmatic ophiolite" rather than to a Penrose-type ophiolite (i.e. it lacks of a continue and complete oceanic crust). The end of the rifting period was marked by deposition of the Radiolarian Chert Formation. During the Cretaceous, the subduction of the European plate beneath the African plate led to the closure of the former Alpine Tethyan realm. The continental collision implied crustal thickening through W-NW-vergent nappe stacking (D1 phase, Froitzheim et al., 1994). The Platta nappe was only affected by a low-temperature prehnite-pumpellyite metamorphism ( $< 300^\circ\text{C}$ ; Dunnoyer de Segonzac and Bernoulli, 1976; Ferreiro-Mahlmänn, 1995). During the Late Cretaceous, a D2 extensional Alpine phase occurred. It produced top-

to-the-east to southeast normal faults (Froitzheim et al., 1994). This event is poorly constrained in the Platta nappe (Epin et al., 2019, Coltat et al., *under revision*). During the Cenozoic, N-S-oriented shortening (D3 phase) resulted in the formation of large-scale E-W folds and N-vergent thrusts (Epin et al., 2017).

Extensional tectonics during Jurassic mantle exhumation was accompanied by intense fluid circulation. This is recorded through i) hydration of primary mantle rocks (i.e. serpentinization) under retrograde conditions (Müntener et al., 2010), ii) alteration of mafic rocks (e.g. rodingitization of mafic intrusions and epidotization-chloritization of mafic extrusive rocks, Amann et al., 2019), iii) formation of mineralized systems (Dietrich, 1972; Perseil-Latouche et al., 1989; Coltat et al., 2019b) and iv) carbonation of serpentinites and basalts (Coltat et al., 2019a, b). HT ultramafic-hosted mineralized systems have been recognized in the Platta nappe (Marmorera-Cotschen area) in the vicinity of a Jurassic extensional detachment (figure 1D, E). Coltat et al. (2019b) interpreted this mineralized system as an equivalent to the root zone of present day ultramafic-hosted black smokers as those active at slow-spreading Mid-Oceanic Ridges. These authors showed that the overall system underwent a certain amount of unroofing during the Alpine orogeny without strong internal deformation. This allows the Jurassic extensional structures to be restored and the mineralized system to be studied in its undisturbed geometry.

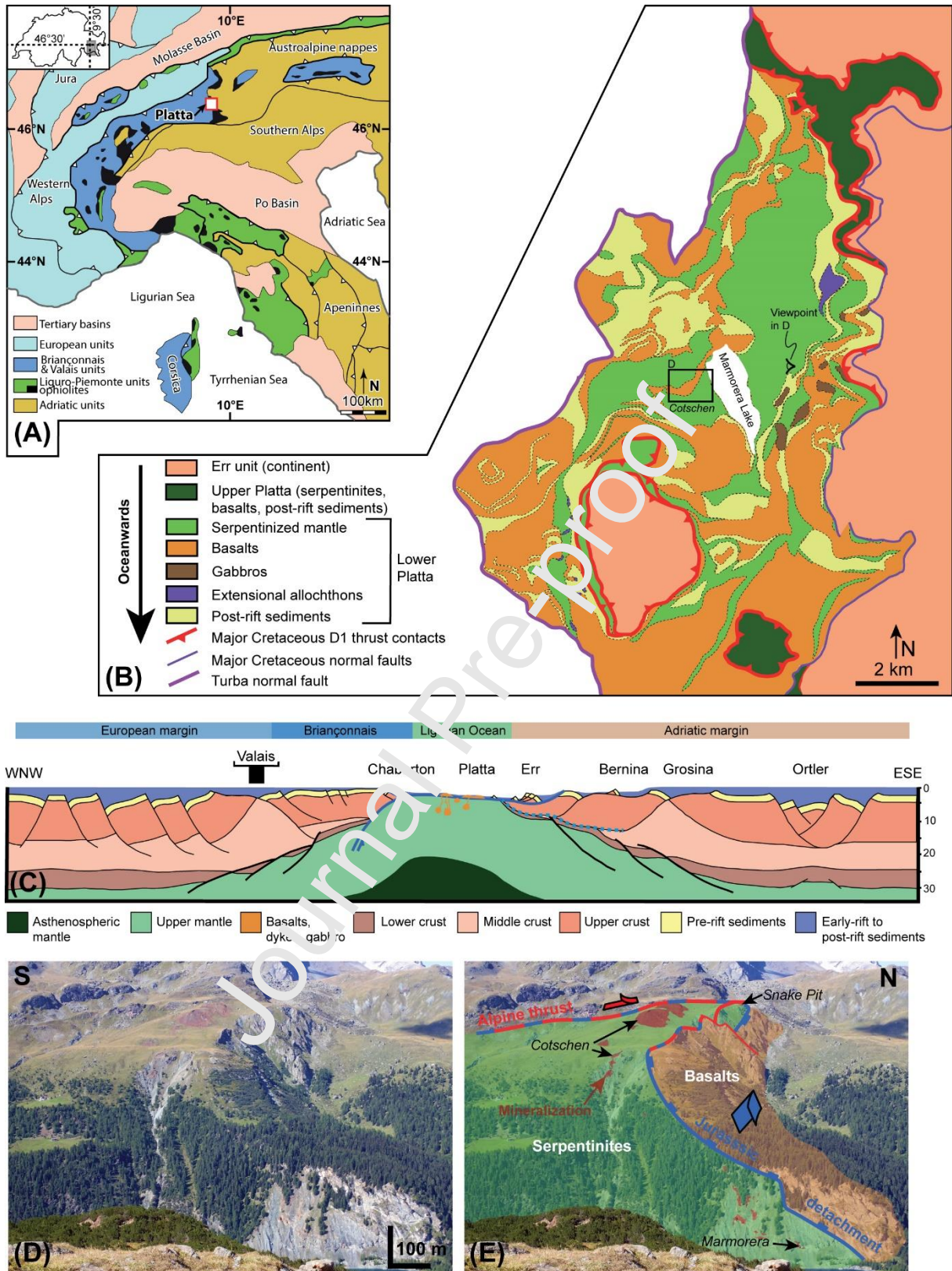


Figure 1. (A) Simplified map showing the main paleogeographic units of the Central and Western Alps and the Apennines. The inset in the top-left corner displays the location of the investigated site in Switzerland. (B) Geological map of the Platta nappe (modified after Schaltegger et al., 2002) showing the Marmorera-Cotschen area displayed in D (black inset).

(C) Restored cross section showing mantle exhumation beneath the Adriatic plate during the Jurassic WNW-ESE-oriented opening of the Alpine Tethys Ocean (after Pinto et al., 2015). (D) Westwards view of the Marmorera-Cotschen hydrothermal system cliff (viewpoint shown in B) and (E) interpreted line-drawing. Modified after Coltat et al. (2019b)

### 3. Sampling, Samples and Analytical methods

#### 3.1. Field description

Coltat et al. (2019b) investigated the Marmorera-Coschen hydrothermal system. A brief description of their results is given here. The MCHS is hosted in the serpentinized footwall of a top-to-the-W detachment juxtaposing basalts onto serpentinites (figure 1D, E, 2A). The system outcrops noticeably well in 3D over a height of 600m. The Fe-Cu-Ni-Co-Zn mineralization is carried by sulfides (mainly chalcopyrite, pyrrhotite, pentlandite, sphalerite), oxides (magnetite) and is associated with coeval Fe-Ca-silicates (ilvaite, hydrogarnet and diopside). As a rule, where mineralization occurs, the primary lizardite is replaced by Fe-antigorite and/or greenalite.

The site of Cotschen represents the bottom of the system, at around 150m below the paleo detachment (figures 1D, E, 2). It is made of serpentinites extensively replaced by Fe-Ca-silicates, sulfides (sphalerite, chalcopyrite, pyrrhotite) and magnetite. Locally, Fe-Ca-silicates veins form a stockwork. At other places, Fe-Ca-silicates are absent and the mineralization is carried by an assemblage of sulfides and oxides in various proportions forming the semimassive sulfides facies. At Cotschen, the end-members of this facies are either sulfide veins (mainly pyrrhotite with minor chalcopyrite) crosscutting serpentinite or serpentinite replaced by magnetite with minor sulfides (figure 2C).

The mineralization of Marmorera is located at around 80m below the detachment (figures 1D, E, 2). The hydrothermal facies from this site are the most diversified among those found at the MCHS (figure 2C). The mineralization is associated with a mafic dyke (figure 2). Close to the dyke, serpentinite is locally almost completely replaced by a Cu-rich assemblage of chalcopyrite and minor isocubanite. Magnetite, pyrrhotite and pentlandite occur together with diopside and are embedded in the chalcopyrite groundmass. Serpentinite clasts locally remain (figure 2C). Where hydrothermal alteration is less intense, a semimassive sulfides facies occurs. It is comprised of pyrrhotite, magnetite and minor chalcopyrite veins. In the serpentinite groundmass, magnetite grown at the expense of Cr-rich spinel is common (figure 2C). Pyrrhotite is locally associated with this magnetite. Fe-Ca-silicates occur in the outer part

of the mineralization. They are comprised of either diopside or magnetite forming infilling pockets and veins, respectively (figure 2C). Ilvaite occurs as veins associated with diopside and minor chalcopyrite and magnetite. Magnetite also occurs in the serpentinite groundmass where it rims spinel relics. Locally, ilvaite rim develops around this magnetite. Barren serpentinite consists of lizardite-rich serpentinite which contains micrometer-sized magnetite and pentlandite grains (figure 2C).

The Snake Pit mineralization is at around 30m below the detachment (figure 2). There, Fe-Ca-silicates vanish (figure 2B) and the mineralization is made of euhedral pyrite forming disseminated grains or aggregates (figure 2C). Inclusions of chalcopyrite, pyrrhotite and sphalerite locally occur in pyrite. These phases together with pentlandite are also encountered around pyrite grains (figure 2C). The mineralization is crosscut by calcite veins forming fracture-filling ophicalcites. Locally, chalcopyrite is associated with calcite suggesting that the copper stock has been slightly remobilized during carbonation (figure 2C).

### 3.2. Sampling strategy

Several samples have been collected at each of the three levels depicted above as representative of the variability of hydrothermal rocks (figure 2C). They represent either serpentinites extensively replaced by Fe-Ca-silicates and/or mineralization (sulfides and oxides) or serpentinites crosscut by mineralized veins (i.e. stockwork structure). The former contains more metal-bearing phases, hence it was mainly investigated. At Snake Pit, the mineralization type differs and is expressed as disseminated sulfides. Also, barren serpentinite has been collected to yield the first-order geochemical signature of the host rocks.

The variability of hydrothermal rocks reported at the MCHS is more important than the one expected at present-day hydrothermal venting sites where massive sulfides rather occur (i.e. Fe-Ca-silicates-rich hydrothermal facies have never been recovered in present-day settings). At the seafloor, where fluids vent, massive sulfides directly precipitate from hydrothermal fluids (i.e. chimneys, sulfide mounds), whereas at the MCHS replacement process of serpentinite by mineralization is the main process of metal enrichment. Therefore, a direct comparison of the geochemical signatures of the two systems (i.e. the MCHS and present-day SMS) would be meaningless. Thus, we first document the element mobilities associated with hydrothermal alteration and mineralization formation at the MCHS. Then we compare these signatures to the ones of present-day deeply altered and mineralized rocks where replacement processes occur.

Noticeably, at the MCHS we do not have evidence of exhalative system. Also, the precise location of the paleo-seafloor remains speculative and the exact basalt thickness is unknown. Therefore, we cannot precisely define the paleodepth of the MCHS. As a consequence, in figure 2B, present-day black smokers represent the termination of the hydrothermal system without spatial continuation with the MCHS. This justifies the horizontal white area in figure 2B. However, we assume that fluids would eventually have vented at the seafloor where SMS likely formed. The strategy adopted in this study was to document the distribution of selected elements on the vertical scale as markers of the processes likely to occur during hydrothermal fluid flow.

Finally, we aim at deciphering, at a given depth, the small-scale hydrothermal processes. To resolve this point, we paid a special attention to the Marmorera section as it displays the largest variety of mineralization types.

### 3.3. Samples

Whole rock chemical analyses on both mineralized and barren samples coupled to in-situ LA-ICPMS analyses on metal-bearing phases (chalcopyrite, pyrrhotite and magnetite) have been carried out.

At the bottom of the system (i.e. Cotscien), two samples of the Fe-Ca-silicates facies have been selected (Cot18\_40a and Cot18\_46b, figure 2C). Both represent serpentinites extensively replaced by an assemblage of Fe-Ca-silicates associated with minor sulfides. The sample Cot18\_46b displays the highest degree of alteration. At the same place, two samples of semimassive sulfides facies have been collected (figure 2C). They correspond to the endmembers of this facies, representing either a pyrrhotite-rich sample (Cot18\_71) or a magnetite-rich with minor sulfides sample (Cot16\_61, figure 2C).

At Marmorera, four samples have been collected perpendicular to a mafic dyke (figure 2C). They correspond to the barren serpentinites (Mar16\_31), the Fe-Ca-silicates facies (Mar18\_39), the semimassive sulfides facies (Mar18\_31a) and the Cu-rich massive sulfides facies (Cu-rich MS, Mar16\_35). An additional sample in the Cu-rich MS (Mar16\_34) has been selected for the determination of the whole rock composition. It corresponds to the most mineralized Cu-rich sample (table 2).

At the top of the system (Snake Pit), four samples have been selected (figure 2C, table 1). Samples Cot16\_49a and Cot16\_52 represent the least and the most mineralized sample, respectively (figure 2C). The four samples also display variable intensity of carbonation.

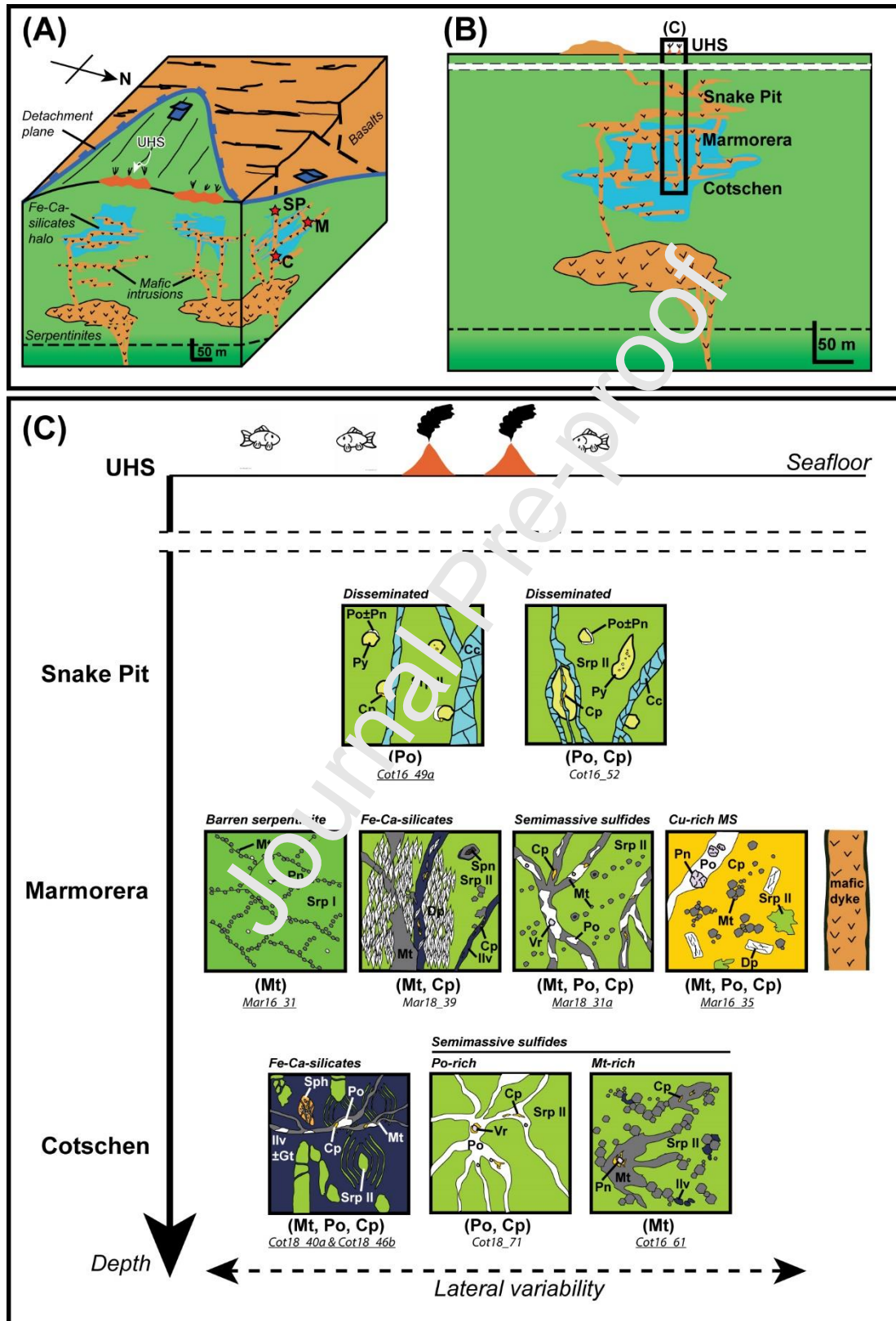


Figure 2. (A) Schematic 3D block diagram showing a detachment fault exhuming mantle rocks beneath a mafic extrusive crust (from Coltat et al., 2019b). Location of the investigated sites (Cotschen, C; Marmorera, M and Snake Pit, SP) at different depths beneath the detachment. (B) Reconstructed section across the mineralized footwall of the paleo detachment of Marmorera-Cotschen. The different sites have been projected from their horizontal position on a vertical section consistently to their paleo-depth. Present-day ultramafic-hosted black smokers (UHS) are displayed at the seafloor. (C) Hydrothermal facies investigated at different structural positions (Cotschen, Marmorera, Snake Pit) through LA-ICPMS analyses. Thin section schemes are unscaled. Below each scheme, the name of the sample and the metal-bearing phases analyzed by LA-ICPMS are given. Underlined samples have been also analyzed through whole rock geochemistry. *Cp*=chalcopyrite, *Po*=pyrrhotite, *Mt*=magnetite, *Pn*=pentlandite, *Py*=pyrite, *Vr*=violaite, *Sph*=sphalerite, *Ilv*=ilvaite, *Gt*=hydro-andradite, *Dp*=diopside, *Srp*=serpentine.

### 3.4. Analytical methods

Whole rock quantitative chemical data were acquired using X-ray fluorescence at the Marine Geosciences department at Ifremer institute (Plouzané, France). Analyses were conducted with a wavelength dispersive X-ray fluorescence spectrometer (WD-XRF; BRUKER AXS S8 TIGER) on fusion beads or compressed pellets for major and trace elements, respectively. Fusion beads were prepared as following. For sulfide-rich rocks 0.3g of dried sample (70°C) was placed in a Pt-Au crucible with 7g spectroflux 161 (Li<sub>2</sub>B<sub>4</sub>O<sub>7</sub> 90% + LiNO<sub>3</sub> 10%; Claisse –Malvern Panlaytical). 3g of NaBr with 3g of spectroflux 161 and 3g of spectroflux 106 (Li<sub>2</sub>B<sub>4</sub>O<sub>7</sub> 85% + Li<sub>2</sub>CO<sub>3</sub> 15%; Johnson Matthey) was then added and the Pt-Au crucible was heated progressively from room temperature to 500°C for 1h in an electric furnace before fusion at 1000°C. This method prevents sulfur loss present in sulfides during fusion at 1000°C. For silicate rocks, 0.5g of calcined sample was placed in a Pt-Au crucible with 9g of spectroflux 120A (Li<sub>2</sub>B<sub>4</sub>O<sub>7</sub> 90% – LiF 10%, SPCSciences) and 500µL of a 250 g/L solution of LiBr (Merck) no-wetting agent was added. The fusion was performed at 1050°C in an electric furnace. Gold was determined after separation on an ion-exchange filter following the methodology described in Etoubleau et al. (1996). After data acquisition, measured net peak intensities corrected from inter-element effects were converted into concentrations using calibration curves generated from the analysis of certified geochemical standard powders prepared following the same protocol and measured under identical analytical conditions. Calibration curves were established using certified rock materials from the Centre de

recherches pétrographiques et géochimiques (e.g. BE- N, IF- G), the Canadian certified reference materials project (e.g. UM- 1, UM- 2, UM- 4, WMG- 1, CCU-1 set, CZN set, KC- 1a, PTC-1a, PTM-1a, RTS-1, RTS-2, RTS-3, MP-1, MP-2, WMS-1a ) and the Geological survey of Japan (e.g. JB- 3, JCFA- 1, JLS- 1, JSD- 2). Reference serpentinite (HARZ01-GeoPT) and Cu-rich sulfide matrix (CCU1d) were analyzed as unknowns using the same methods as for the silicate and sulfur samples, respectively (appendix 6).

Prior to LA-ICPMS analyses, the sulfides and oxides were analyzed using a Cameca SX100 Electron Probe Micro Analyser (EPMA) at Microsonde Ouest (Plouzané, France) to give composition used for internal standard. Analyses were conducted using an accelerating voltage of 15kV and a beam current of 20nA. A beam diameter of 5 and 1  $\mu\text{m}$  was used for analyses on sulfides and oxides, respectively. Natural sulfides and oxides standards have been used for standardization. Counting time for sulfides was 10s for S, Fe, Co, Cr, Ni, Ti and Mn; 20s for Cu, Zn, and Se; 60s for As and V. For magnetite, counting time was 10s for all element except Zn was 20s.

After optical microscopy and EPMA analysis selected samples were analysed by laser ablation quadrupole inductively coupled plasma mass spectrometry (LA-Q-ICPMS) at Trinity College, Dublin. Trace element analysis was carried out using a Teledyne-Cetac G2 193 nm wavelength ArF excimer laser ablation system with a HelEx 2-volume cell, where ablation occurs. The laser is coupled via extremely narrow bore PEEK tubing and a Teledyne-Cetac ARIS rapid sample-introduction system to a Thermo-Fischer iCap Qs quadrupole ICPMS. This analytical set-up is ideal for rapid elemental mapping. For spot analyses an in-house adjustable-volume signal-smoothing device was used, which permitted the use of a wide range of laser repetition rates.

The primary standard material used is USGS MASS-1 sulphide (Wilson et al., 2002). UQAC sulphide micropowder pellet (Onuk et al., 2017), MUL sphalerite (Onuk et al., 2017) and basalt glass BCR-2G were the secondary standards employed (appendix 7). Conventional standard-sample bracketing was used during spot analysis. Data reduction was performed using the Iolite data reduction software (Paton et al., 2011). After the data treatment, each individual integration was checked for where spikes in the signal due to microinclusions or mechanical mix between distinct sulfide phases (e.g. change of phase with increasing ablation depth) were clearly recognized, the analyses were dismissed to avoid the effect of mineralogical inclusions in the analyzed phase. Average mineral Fe composition data from

EPMA analyses were used as the necessary internal standard for the processing of the spot trace element data acquired via LA-ICP-MS.

#### 4. Results

The whole rock and single grain chemical compositions are given in tables 1 to 5 and are represented in figures 3 to 13 for selected elements. The extensive data base is presented as discriminants diagrams in appendix 1 and box plots in appendixes 2 to 4.

Although Fe-Ca-rich metasomatism was coeval to mineralization at the MCHS, we differentiate between the two processes. Throughout the manuscript, “altered rocks” refer to serpentinites replaced by Fe-Ca-silicates (and locally associated with minor sulfides), whereas “mineralized rocks” correspond to serpentinites replaced by metal-bearing phases (sulfides and oxides). The most altered rocks do not necessarily correspond to the most mineralized but rather reflect higher degree of hydrothermal alteration underwent by the serpentinites.

Table 1. Whole rock major and trace element compositions of barren, altered and mineralized rocks from the MCHS and averaged compositions of rocks at the present-day ultramafic-hosted Rainbow hydrothermal site.

Cotschen		Marmorera		Snake Pit			Rainbow <sup>a</sup>	Rainbow <sup>b</sup>		Stockwork	Steatite	
Fe-Ca-silicates		Semi. Sulf.	Barren serp.	Semi. Sulf.	Disseminated mineralization			Barren serp.	Barren serp.	k	e	
Cot18_40 a	Cot18_46 b	Cot16_61	Mar16_31	Mar18_31 a	Cot16_49 a	Cot16_5 4	Cot16_5 5	n=12	n=7	n=7	n=3	
46°29'56N		46°29'54 N	46°30'18N	46°30'02N								
9°37'16E		9°36'58E	9°37'40E	9°36'42E								
<i>Elements given in wt. %</i>												
SiO <sub>2</sub>	34.5	28.52	29.83	38.35	32.99	31.67	26.77	29.84	38.07	37.06	30.36	55.93
Al <sub>2</sub> O <sub>3</sub>	2.25	1.09	0.99	0.52	1.35	1.38	1.7	2.08	0.67	0.70	0.33	0.18
MgO	21.48	12.14	21.35	38.54	25.5	29.25	24.34	27.7	37.09	38.07	27.97	25.83
MnO	0.48	0.45	0.23	0.08	0.2	0.42	0.85	0.63	0.08	0.09	0.11	0.01
TiO <sub>2</sub>	0.09	0.05	<0.05	<0.05	<0.05	<0.05	0.05	0.05	0.013	0.009	0.003	<0.001
CaO	5.98	7.1	0.25	<0.1	0.02	10.63	14.27	12.11	1.12	1.07	1.49	<0.01
Fe <sub>2</sub> O <sub>3</sub>	27.44	46.45	39.66	7.98	30.81	7.16	8.84	7.05	8.71	7.24	16.87	9.14
Na <sub>2</sub> O	<0.1	<0.1	<0.1	<0.1	<0.1	<0.1	<0.1	<0.1	0.17	0.16	0.38	0.20
K <sub>2</sub> O	<0.05	<0.05	<0.05	<0.05	<0.05	<0.05	<0.05	<0.05	0.06	0.04	0.06	0.01
P <sub>2</sub> O <sub>5</sub>	<0.05	<0.05	<0.05	<0.05	<0.05	<0.05	<0.05	<0.05	0.04	0.02	0.01	<0.01
S	-	-	0.6	-	1.3	-	3.8	1.6	-	0.06	5.28	0.70
LOI	7.3	4.3	6.9	12.6	8.7	16.6	15.8	16.8	14.12	14.41	16.16	4.48
<i>Elements given in ppm</i>												
Sc	<10	<10	<10	<10	19	<10	<10	13	-	6.6	4.6	2
V	53	42	35	22	72	37	53	64	-	28	14	9
Cr	1750	1060	1880	2780	3060	1900	2510	2020	-	2162	1852	650
Co	131	82	200	98	170	54	158	80	104	104	139	249

Ni	1450	203	1090	2250	2430	1170	1890	1750	1846	1658	1022	652
Cu	1380	3900	11700	48	270	11	5600	1140	20	542	1421	257
Zn	142	757	113	21	146	38	3440	504	127	149	527	222
As	<10	<10	<10	<10	<10	<10	<10	<10	6.1	3.4	1.9	0.65
Rb	<5	<5	<5	<5	<5	<5	<5	<5	0.21	<1	2	<1
Sr	<10	<10	<10	<10	12	185	192	117	205	74	219	<1
Y	<5	<5	<5	<5	<5	<5	<5	<5	0.44	1	1	<0.5
Zr	10	11	8	5	7	5	6	<5	-	5.7	4.4	2
Nb	<2	<2	<2	<2	<2	<2	<2	<2	-	<0.2	0.78	0.3
Mo	<10	<10	<10	<10	<10	<10	<10	<10	-	<2	9.8	5.3
Ag	-	-	<50	-	-	-	<50	-	-	<0.5	0.93	<0.5
Sb	<20	<20	<20	<20	<20	<20	<20	<20	0.14	0.6	0.47	0.10
Ba	<100	<100	<100	<100	<100	<100	<100	<100	0.9	2	4.2	2
Au	-	-	<0.1	-	-	-	<0.1	-	-	0.004	0.044	0.011
La	<20	<20	<20	<20	<20	<20	<20	<20	1.1	-	-	-
Ce	<20	<20	<20	<20	<20	<20	<20	<20	1.27	-	-	-
Pb	<10	<10	<10	<10	<10	<10	<10	<10	0.5	<5	7.3	4

<sup>a</sup>from Andreani et al. (2014)

<sup>b</sup>from Marques et al. (2007)

Abbreviations: Semi. Sulf.=semimassive sulfides; Barren serp.=barren serpentinite. "-"=element not measured.

Table 2. Major and trace element compositions of the Cu-rich MS at the MCHS compared to averaged compositions of selected present-day SMS (from Fouquet et al., 2010 and references therein).

	MCHS		UHS		MHS				
	Marmorera		Rainbow 1	Logatchev 1	Ashasze 1	TAG	Krasnov	Lucky Strike	
	Mar16_34	Mar16_35	n=116	n=40	n=49	n=34	n=16	n=154	
	46°30'18N								
	9°37'40E								
	<i>Elements given in wt. %</i>								
S	35.13	24.48	32.75	26.36	21.74	35.21	42.9	30.97	
Fe	36.28	36.22	28.56	24.4	32.81	24.89	38.96	21.05	
Zn	0.28	0.28	14.99	2.55	14.11	13.38	0.14	4.16	
Cu	27.72	13.8	12.43	25.47	14.21	7.77	2.21	5.37	
Ca	<0.1	1.5	2.69	2.56	1.13	5.38	1.61	2.7	
Ba	<0.05	<0.05	0.29	0.06	0.05	0.47	0.27	10.85	
SiO <sub>2</sub>	0.01	10.49	0.71	4.44	1.3	12.83	11.21	12.38	
MgO	0.27	4.85	-	-	-	-	-	-	
	<i>Elements given in ppm</i>								
Co	990	1580	5086	500	2882	643	628	89	
Ni	2170	2400	490	92	973	22	15	10	
Ga	<10	<10	-	23	32	116	21	-	
Ge	<25	<25	12	12	10	22	<5	17	
As	33	18	214	62	231	62	66	334	
Se	82	<20	186	625	200	159	23	110	
Sr	<20	<20	665	293	31	412	602	2208	
Mo	<10	<10	29	51	31	144	88	79	
Ag	119	84	188	35	79	114	18	74	
Cd	<20	<20	391	51	251	549	19	195	
In	<20	<20	10	8	11	<10	10	1	
Sn	<20	<20	138	225	347	<20	23	1	
Sb	<20	<20	34	21	29	229	20	28	

Au	<0.1	0.8	5.1	8.4	6.3	1.4	1.1	0.3
Pb	<1000	<1000	342	209	350	214	70	530
U	<20	<20	11	14	7	9	11	<5

"-"=element not measured. UHS=Ultramafic-hosted hydrothermal systems. MHS=Mafic-hosted hydrothermal systems

Journal Pre-proof

Table 3. LA-ICPMS trace element compositions of chalcopyrite (in ppm) of the fossil MCHS and present-day VMS.

Element	Accuracy* (%)	System	MCHS				MHS	UHS	
			Cotschen	Marmorera		Snake Pit			
		Structural level							
		Hydrothermal facies	Semimassive sulfides	Fe-Ca-silicates	Semimassive sulfides	Cu-rich MS	Disseminated mineralization		
	Sample (number of analyses)	Cot18_71 (18)	Mar18_39 (12)	Mar18_31a (16)	Mar16_35 (20)	Cot16_52 (34)			
Cr	5	Median	2.2	75	4.55	1.4	5.8	-	-
		2 $\sigma$	4.40	30.7	1.51	1.20	2.03	-	-
		<i>Min-Max</i>	<i>1.6-16</i>	<i>23.8-538</i>	<i>1.56-8.9</i>	<i>1.4-1.4</i>	<i>3.8-14.8</i>	-	-
Mn	16	Median	23.1	17.6	30.5	10.55	26.75	2.98	-
		2 $\sigma$	12.6	5.44	7.16	3.34	23.8	-	-
		<i>Min-Max</i>	<i>6.2-230</i>	<i>1.5-56</i>	<i>10.5-83</i>	<i>4.3-30</i>	<i>9.7-1020</i>	<i>0.67-13</i>	-
Co	7	Median	16.9	3.2	6.9	2.14	3.9	75.2	-
		2 $\sigma$	42.4	1.13	24.0	6.90	6.69	-	-
		<i>Min-Max</i>	<i>0.88-109.1</i>	<i>0.93-14.1</i>	<i>0.66-630</i>	<i>0.41-211</i>	<i>0.85-180</i>	<i>2.45-370</i>	-
Ni	4	Median	434.5	38.75	188.5	8.25	21.45	20.96	-
		2 $\sigma$	142	10.7	157	58.6	56.4	-	-
		<i>Min-Max</i>	<i>71-2800</i>	<i>15-207</i>	<i>5.3-4000</i>	<i>2.5-2250</i>	<i>4.2-720</i>	<i>0.38-40.4</i>	-
Zn	57	Median	84	164.5	359.5	318	342.5	121.9	-
		2 $\sigma$	228	39.5	549	109	85.0	-	-
		<i>Min-Max</i>	<i>31-7300</i>	<i>105-473</i>	<i>176-3800</i>	<i>153-1180</i>	<i>186-2360</i>	<i>8.61-25896</i>	-
Ga	4	Median	0.18	0.62	0.16	bdl	bdl	6.105	-
		2 $\sigma$	0.13	0.25	0.12	bdl	bdl	-	-
		<i>Min-Max</i>	<i>0.13-0.18</i>	<i>0.62-0.62</i>	<i>0.099-0.42</i>	<i>bdl</i>	<i>bdl</i>	<i>1-183.5</i>	-
Ge	45	Median	1.9	bdl	1.19	1	bdl	15	-
		2 $\sigma$	1.90	bdl	0.66	0.73	bdl	-	-
		<i>Min-Max</i>	<i>1.9-1.9</i>	<i>bdl</i>	<i>0.83-1.31</i>	<i>0.95-1.09</i>	<i>bdl</i>	<i>3.02-75.1</i>	-

As	12	Median	1.97	bdl	1.85	2.1	3.08	3.81	49.45
		2 $\sigma$	2.62	bdl	1.09	1.30	1.29	-	-
		<i>Min-Max</i>	<i>1.3-4.3</i>	<i>bdl</i>	<i>1.25-4.5</i>	<i>2.1-2.1</i>	<i>1.71-10.9</i>	<i>0.297-2873</i>	<i>3.86-572</i>
Se	27	Median	15.2	13.5	12.8	12.5	26.65	156	606
		2 $\sigma$	2.53	2.00	2.18	2.26	3.02	-	-
		<i>Min-Max</i>	<i>3.2-31</i>	<i>9.6-19.1</i>	<i>8.1-15.5</i>	<i>10.4-15.8</i>	<i>23.2-35.2</i>	<i>9.25-852.5</i>	<i>22.5-1510</i>
Mo	7	Median	bdl	bdl	bdl	0.2	30	1.49	-
		2 $\sigma$	bdl	bdl	bdl	0.49	11.8	-	-
		<i>Min-Max</i>	<i>bdl</i>	<i>bdl</i>	<i>bdl</i>	<i>0.13-1.3</i>	<i>0.34-593</i>	<i>0.027-4497</i>	-
Ag	67	Median	0.476	1.42	1.215	7.08	1.69	16.7	-
		2 $\sigma$	0.25	0.45	0.17	0.57	0.38	-	-
		<i>Min-Max</i>	<i>0.22-2.7</i>	<i>0.285-9.9</i>	<i>0.122-3.51</i>	<i>2.73-29.3</i>	<i>0.126-13</i>	<i>1.48-243</i>	-
Cd	436	Median	4.4	bdl	4.2	4.9	5.7	3.369	-
		2 $\sigma$	3.49	bdl	1.70	2.17	1.72	-	-
		<i>Min-Max</i>	<i>2-24.2</i>	<i>bdl</i>	<i>1.8-19.5</i>	<i>1.6-10.2</i>	<i>3-12.4</i>	<i>0.064-89</i>	-
In	17	Median	0.341	0.02	5.75	9.67	0.62	5.18	-
		2 $\sigma$	0.09	0.23	0.30	0.52	0.07	-	-
		<i>Min-Max</i>	<i>0.032-1.15</i>	<i>0.42-1.19</i>	<i>1.99-6.64</i>	<i>7.57-13.04</i>	<i>0.4-0.99</i>	<i>0.3-52.8</i>	-
Sn	18	Median	0.66	bdl	0.38	0.66	0.45	15	-
		2 $\sigma$	0.24	bdl	0.27	0.43	0.31	-	-
		<i>Min-Max</i>	<i>0.02-15</i>	<i>bdl</i>	<i>0.38-0.42</i>	<i>0.45-1.05</i>	<i>0.44-0.65</i>	<i>0.866-232.3</i>	-
Sb	12	Median	1.06	bdl	0.43	bdl	0.45	0.15	6.37
		2 $\sigma$	0.75	bdl	0.20	bdl	0.21	-	-
		<i>Min-Max</i>	<i>1.06-1.06</i>	<i>bdl</i>	<i>0.3-0.73</i>	<i>bdl</i>	<i>0.37-1.83</i>	<i>0.005-35</i>	<i>0.6-198</i>
Te	-	Median	2.095	0.62	1.01	2.93	bdl	5.315	54.45
		2 $\sigma$	0.71	0.24	0.41	0.71	bdl	-	-
		<i>Min-Max</i>	<i>0.55-10.2</i>	<i>0.42-1.19</i>	<i>0.74-1.66</i>	<i>1.08-5.19</i>	<i>bdl</i>	<i>1.16-63</i>	<i>1.18-153</i>
Pt	43	Median	bdl	bdl	bdl	bdl	bdl	-	-
		2 $\sigma$	bdl	bdl	bdl	bdl	bdl	-	-
		<i>Min-Max</i>	<i>bdl</i>	<i>bdl</i>	<i>bdl</i>	<i>bdl</i>	<i>bdl</i>	-	-

Au	-	Median	bdl	bdl	0.49	bdl	0.093	0.314	2.035
		2 $\sigma$	bdl	bdl	0.89	bdl	0.09	-	-
		<i>Min-Max</i>	<i>bdl</i>	<i>bdl</i>	<i>0.49-0.49</i>	<i>bdl</i>	<i>0.07-0.23</i>	<i>0.06-2.55</i>	<i>0.04-11.6</i>
Pb	10	Median	3.925	6.48	5.175	2.79	6.7	0.383	-
		2 $\sigma$	0.78	0.67	0.61	0.52	0.82	-	-
		<i>Min-Max</i>	<i>0.69-8.58</i>	<i>1.81-14.5</i>	<i>1.02-8.89</i>	<i>0.56-8.6</i>	<i>0.46-20.3</i>	<i>0.06-2.55</i>	-
Bi	13	Median	0.063	0.108	0.234	0.065	0.073	0.106	-
		2 $\sigma$	0.09	0.02	0.06	0.05	0.02	-	-
		<i>Min-Max</i>	<i>0.039-0.41</i>	<i>0.032-0.243</i>	<i>0.047-0.766</i>	<i>0.025-0.2</i>	<i>0.029-0.16</i>	<i>0.002-2.31</i>	-

Values below the limits of detection are not considered. Abbreviations: bdl=below the detection limit

MHS data are from Wohlgemuth et al., 2015; Melekestseva et al., 2017; Grant et al., 2018; Luque et al., 2018.

UHS data are from Wohlgemuth et al., 2015.

\*Average of the differences measured between the known element content of the international standard BCR or MUL1 (As and Se) and the content obtained running the standard as an unknown (relative error).

Table 4. LA-ICPMS trace element compositions of pyrrhotite (in ppm) of the fossil MCHS

Element	Accuracy* (%)	Structural level Hydrothermal facies	Cotschen		Marmorera	Cu-rich MS	Snake Pit	
			Fe-Ca-silicates	Semimassive sulfides	Semimassive sulfides		Disseminated mineralization	
		Sample (number of analyses)	Cot18_40a (8)	Cot18_71 (59)	Mar18_31a (57)	Mar16_35 (59)	Cot16_49a (6)	Cot16_52 (8)
Cr	6	Median	bdl	2	4.85	3.3	5	4.1
		2 $\sigma$	bdl	0.69	2.23	3.70	5.62	2.40
		<i>Min-Max</i>	<i>bdl</i>	<i>0.8-12</i>	<i>2.9-11.1</i>	<i>3.3-3.3</i>	<i>2.6-159</i>	<i>4.1-4.1</i>
Co	13	Median	171	152	61.95	100.85	15.45	56.4
		2 $\sigma$	21.6	31.2	22.7	17.2	4.98	7.03
		<i>Min-Max</i>	<i>123-272</i>	<i>42-2900</i>	<i>29.6-750</i>	<i>14.4-1140</i>	<i>10.5-152</i>	<i>31.5-93.5</i>
Ni	13	Median	110	2080	2755	813.5	3640	1599
		2 $\sigma$	50.9	82	322	95.7	323	132
		<i>Min-Max</i>	<i>11-950</i>	<i>44.8-6720</i>	<i>1490-9400</i>	<i>78-4900</i>	<i>3590-7600</i>	<i>1117-2450</i>
Cu	29	Median	1930	27.4	3.33	40	21	43.5
		2 $\sigma$	515	70.8	8.93	250	20.9	347
		<i>Min-Max</i>	<i>4.1-200</i>	<i>0.98-6490</i>	<i>1.1-213</i>	<i>1.8-5300</i>	<i>3.8-42</i>	<i>3.3-12200</i>
Zn	66	Median	bdl	21	65	100	116.5	35
		2 $\sigma$	bdl	28.9	150	582	172	42.3
		<i>Min-Max</i>	<i>bdl</i>	<i>6.2-250</i>	<i>13.8-140</i>	<i>27-7900</i>	<i>53-180</i>	<i>26-164</i>
Ge	59	Median	bdl	0.99	1.16	0.955	1.075	1.715
		2 $\sigma$	bdl	0.22	0.41	0.63	0.40	0.58
		<i>Min-Max</i>	<i>bdl</i>	<i>0.69-1.56</i>	<i>0.81-3.3</i>	<i>0.58-4.6</i>	<i>0.86-1.69</i>	<i>1.33-2.1</i>
As	16	Median	3	0.68	0.98	4.75	8.1	7.6
		2 $\sigma$	4.40	0.51	0.66	8.25	1.36	2.15
		<i>Min-Max</i>	<i>3.0-3.0</i>	<i>0.56-0.97</i>	<i>0.32-3.59</i>	<i>1.5-8</i>	<i>2.6-13.6</i>	<i>5.7-9.5</i>
Se	12	Median	4.95	2.27	7.98	12.05	28.65	36.2
		2 $\sigma$	1.83	0.77	1.35	2.66	3.22	4.16

Ag	64	<i>Min-Max</i>	3.8-5.6	1.13-18	6.2-10.4	8-18.2	22.3-40.9	31.6-44
		Median	0.97	0.306	0.24	4.98	0.605	1.13
		2 $\sigma$	0.29	0.06	0.10	1.97	0.38	0.24
Sb	13	<i>Min-Max</i>	0.48-3.42	0.055-0.85	0.065-0.93	1.47-97	0.136-1.73	0.439-2.16
		Median	bdl	0.167	2.7	0.52	1.27	0.49
		2 $\sigma$	bdl	0.46	4.54	0.45	0.30	0.28
Pt	41	<i>Min-Max</i>	bdl	0.135-1	0.86-4.4	0.51-0.53	1.27-1.27	0.49-0.49
		Median	bdl	bdl	0.015	0.095	bdl	bdl
		2 $\sigma$	bdl	bdl	0.06	0.70	bdl	bdl
Pb	14	<i>Min-Max</i>	bdl	bdl	0-0.19	0-0.78	bdl	bdl
		Median	2.97	1.56	2.25	5.655	2.91	7.3
		2 $\sigma$	0.59	0.26	0.39	0.94	0.61	1.31
Bi	43	<i>Min-Max</i>	1.65-8.2	0.399-10.28	0.433-8.45	1.74-13	0.71-18.7	3.5-15.6
		Median	0.043	0.0	0.147	0.411	0.06	0.107
		2 $\sigma$	0.02	0.02	0.06	0.10	0.08	0.07
		<i>Min-Max</i>	0.042-0.043	0.016-0.364	0.019-1.5	0.135-1.48	0.06-0.06	0.046-0.12

Values below the limits of detection are not considered. Abbreviations: bdl=below the detection limits

\*Average of the differences measured between the known element content of the international standard BCR or MUL1 (for As and Se) and the content obtained running the standard as an unknown (relative error)

Table 5. LA-ICPMS trace element compositions of magnetite (in ppm) of the fossil MCHS and present-day VMS (data from Patten et al., 2016)

Element	Accuracy* (%)	System	MCHS									MHS
		Structural level	Cotschen					Marmorera				Hole 1256D
		Hydrothermal facies	Fe-Ca-silicates		Semimassive sulfides	Barren serpentine	Fe-Ca-silicates		Semimassive sulfides		Cu-rich MS	Hydrothermal Magnetite
Sample (number of analyses)	Cot18_40a (31)	Cot18_46b (20)	Cot16_61 (20)	Mar16_31 (5)	Mar18_39V (9)	GM (11)	Mar18_31V (16)	GM (24)	Mar16_35 (19)			
Na	10	Median	44	bdl	bdl	bdl	bdl	bdl	43.5	35	21	-
		2 $\sigma$	15	bdl	bdl	bdl	bdl	bdl	10.9	15.7	11.6	-
		Min-Max	44-44	bdl	bdl	bdl	bdl	bdl	28.5-80	18.6-387	15.4-46	-
Mg	7	Median	1120	1190	472	6250	433	325	1111.5	1175	167	-
		2 $\sigma$	364	180	393	345	45.9	71.4	330	290	87.1	-
		Min-Max	167.3-16800	89.6-7900	91-29120	3090-9170	125-1661	104.7-2890	162-7900	88-9860	1490	-
Al	2	Median	55.3	1960	150	33.7	bdl	bdl	34	72	14.4	-
		2 $\sigma$	50.0	550	14.3	5.3	bdl	bdl	23.9	61.4	6.9	-
		Min-Max	12.7-3090	1960-1960	149-2070	14.3-54.3	bdl	bdl	9.5-480	7.1-2440	7.3-102	-
Si	9	Median	8350	bdl	8600	15300	bdl	bdl	15800	16050	9400	-
		2 $\sigma$	2225	bdl	3200	1620	bdl	bdl	1869	2125	1758	-
		Min-Max	4700-35600	bdl	5600-39800	11900-24200	bdl	bdl	12500-25400	11600-37400	5900-13900	-
K	2	Median	bdl	381	bdl	bdl	36	bdl	75.5	68	32.5	-
		2 $\sigma$	bdl	26	bdl	bdl	18	bdl	16.3	18.4	14.3	-
		Min-Max	bdl	381-381	bdl	bdl	36-36	bdl	60-94	28-160	30-61	-
Ti	5	Median	46	bdl	94.8	75.6	122	78.2	109	108	53.7	-
		2 $\sigma$	9.4	bdl	9.8	4.9	9.5	11.8	7.4	29.7	4.6	-
		Min-Max	0.8-917	bdl	7.4-589	63.2-97.1	61.4-226	40.1-226	1.67-537	61.2-1820	164.7	-

V	8	Median	18.4	bdl	66.4	12.5	95.4	94.5	67.5	130	44.5	2580
		2 $\sigma$	1.9	bdl	5.2	1.1	6.3	7.7	4.4	15.3	3.2	-
		<i>Min-Max</i>	3.2-65.8	<i>bdl</i>	5-284	6.14-16.5	59.1-129.9	42.5-184	0.87-173	100.8-541	4.6-97.2	2110-3700
Cr	8	Median	974	5	2705	31.6	1920	9460	5.7	3510	19.1	70
		2 $\sigma$	110	2.1	171	2.3	126	921	1.7	1226	8.06	-
		<i>Min-Max</i>	3.7-13400	4.1-7.5	41-16770	26.7-33.7	38.6-9620	54300	3.3-16.3	84500	3.5-1129	16-314
Mn	5	Median	301	227	230	1077	123	127	194	196	135	-
		2 $\sigma$	26.0	14.5	12.7	35.6	6.11	17.1	15.4	60.1	6.20	-
		<i>Min-Max</i>	235.7-2930	312	179.8-148.7-678	1174	1006-103.1-105.8-	168.3	220	173-809	4700	179.3
Co	5	Median	12.3	17.4	8	15.8	13.1	14.7	12.9	13.5	20.1	-
		2 $\sigma$	1.86	4.02	9.27	0.79	23.6	1.75	0.87	1.18	1.97	-
		<i>Min-Max</i>	4.1-48	8.3-72	5.8-70	11.6-15.3	11.1-130	26.5	10.1-16	12-40.5	33.6	-
Ni	13	Median	47	38.5	18.8	1340	111	97.2	74.9	181	28.7	477
		2 $\sigma$	14.7	4.43	7.34	62.6	29.1	11.4	7.48	11.5	5.58	-
		<i>Min-Max</i>	4.3-600	5.8-60.1	11.9-175	1801	80-250	79.9-164	6.7-138.4	82.2-258	18.2-73	224-1420
Cu	24	Median	1690	116	21.8	6.8	29.2	8.9	4.3	2	28.4	33
		2 $\sigma$	638.4	121.9	128	151	3.70	14.4	71.7	30.5	17.2	-
		<i>Min-Max</i>	1.7-5920	2920	6.9-3500	3.48-370	29.2-29.2	7.8-10	0.94-1080	1.6-70	0.7-163	8-102
Ga	4	Median	0.32	bdl	bdl	0.18	bdl	bdl	0.22	0.25	0.29	-
		2 $\sigma$	0.14	bdl	bdl	0.10	bdl	bdl	0.13	0.12	0.14	-
		<i>Min-Max</i>	0.22-1.29	<i>bdl</i>	<i>bdl</i>	0.18-0.18	<i>bdl</i>	<i>bdl</i>	0.15-0.34	0.14-0.76	0.56	-

Values below the limits of detection are not considered. Abbreviations: V=veins, GM=groundmass, bdl=below the detection limits

\*Average of the differences measured between the known element content of the international standard BHVO or NIST (for Ni) and the content obtained running the standard as an unknown (relative error).

Journal Pre-proof

#### 4.1. Alteration of ultramafic rocks at the MCHS

Altered and mineralized rocks at the MCHS (figure 3A, B) plot outside the range defined by deeply altered and mineralized serpentinites (i.e. stockwork and steatite) beneath the SMS at the Rainbow hydrothermal site (Marques et al., 2007). At the MCHS, the barren serpentinite is close to the serpentinite pole (figure 3A) and mimics the signature of present-day oceanic serpentinites (Marques et al., 2007; Andreani et al., 2014).

Where mineralization occurs in a stockwork structure replacing serpentinites at the Rainbow hydrothermal site, the  $\text{Fe}_2\text{O}_3$  and  $\text{SiO}_2$  contents of the rocks increase and decrease, respectively. This reflects the formation of Fe-rich sulfides and magnetite replacing serpentinite (Marques et al., 2007). Seafloor altered serpentinites are locally characterized by extensive steatitisation (Marques et al., 2007) resulting in their proximity to the talc pole (figure 3A) and the increase of their  $\text{SiO}_2$  content (figure 3B), which is not observed in altered rocks at the MCHS. Rather, a Fe-Ca-rich metasomatism occurred leading to an increase of the  $\text{Fe}_2\text{O}_3$  content of the rocks together with a decrease of the  $\text{SiO}_2$  - CaO content, consistently with the replacement of serpentinites by Fe-Ca-rich silicates. This explains the position of the Fe-Ca-silicates in between the ilvaite and serpentinite poles. The sample Cot18\_46 displays a higher degree of replacement consistently with its closest position to the ilvaite pole. The semimassive sulfides are shifted towards the magnetite pole accordingly to the presence of magnetite replacing serpentine in these facies. As a consequence, the  $\text{Fe}_2\text{O}_3$  content increases and the  $\text{SiO}_2$  content slightly decreases in these samples. Noticeably, the  $\text{Fe}_2\text{O}_3$  content in the altered and mineralized rocks at the MCHS is higher than the one reported in deeply mineralized rocks beneath the Rainbow hydrothermal system.

The carbonated samples from Snake Pit display quite homogenous chemical signatures shifted towards the calcite pole. This leads to an apparent decrease of the  $\text{SiO}_2$ -CaO content without significant enrichment in  $\text{Fe}_2\text{O}_3$ . This carbonation resulted from a low-T (of about 130°C), seawater-derived hydrothermal stage which represents the latest oceanic hydrothermal stage

recorded at the MCHS (Coltat et al., 2019b). The potential remobilization of the former metal stock during this event is discussed below.

At the MCHS, Fe-Ca-rich metasomatism and mineralization formation are accompanied by an increase of the Co/Ni ratio (figure 3C, D). A similar evolution is noticed in the deeply altered and mineralized rocks from the Rainbow hydrothermal site. This peculiarity is less clear in the mineralized rocks from Snake Pit. The high Cu and Zn content increase in mineralized rocks from the MCHS are comparable to the ones reported in deeply mineralized and altered rocks from the Rainbow hydrothermal site. There is no apparent relationship between the Co/Ni ratio and the metal content.

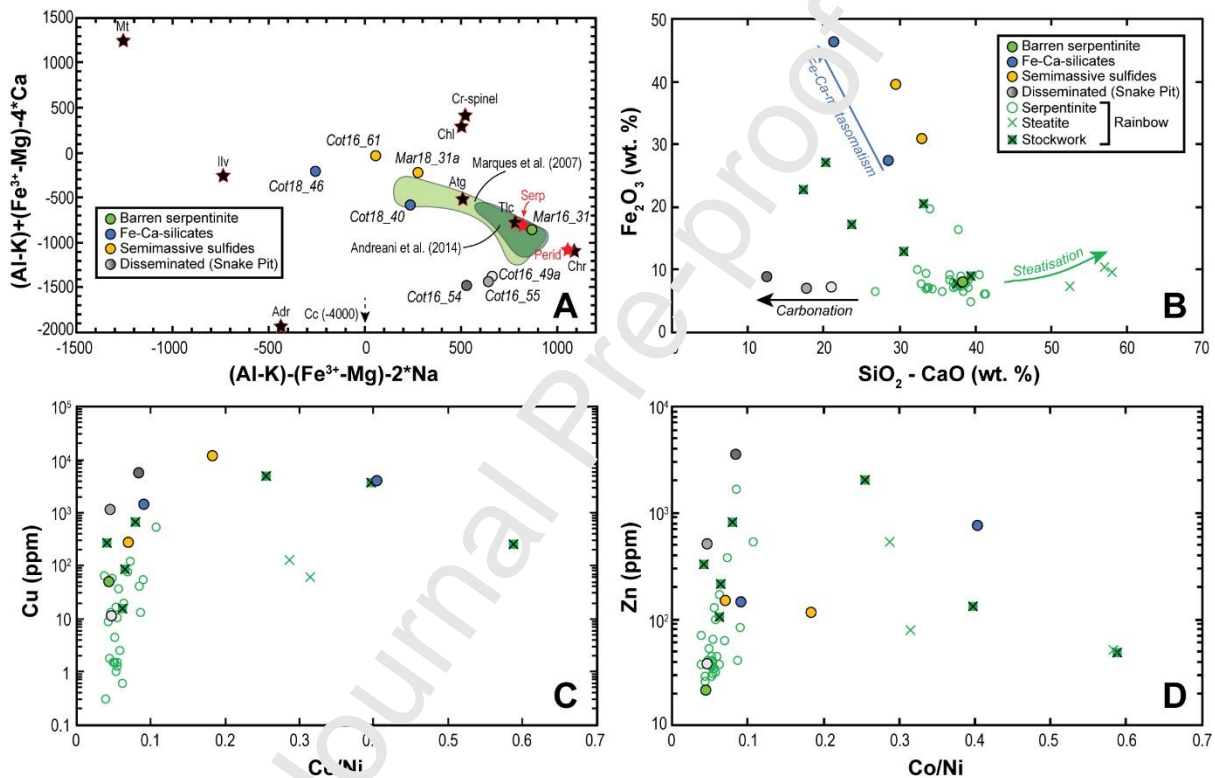


Figure 3. Chemico-mineralogical discriminant diagram (A, after de La Roche and Marchal, 1978), major (B) and trace (C, D) element compositions of the barren, altered and mineralized rocks at the MCHS compared to present-day equivalents (from Marques et al., 2007; Andreani et al., 2014). Mt=magnetite, Atg=antigorite, Ilv=ilvaite, Adr=andradite, Cc=calcite, Chl=chlorite, Tlc=talc, Chr=chrysotile, Serp=serpentinite, Perid=peridotite.

The Cu-rich Massive Sulfides at the MCHS present geochemical signatures similar to the ones of seafloor massive sulfides (table 2) allowing to compare their relative metal enrichments (figure 4). Ultramafic-hosted mineralized systems are characterized by Fe content lower than the one of mafic-hosted mineralization (figure 4). The Cu-rich MS at the

MCHS are between mafic or ultramafic signatures but display a tendency toward high Co content. This is consistent with the mineralization being hosted in ultramafic rocks

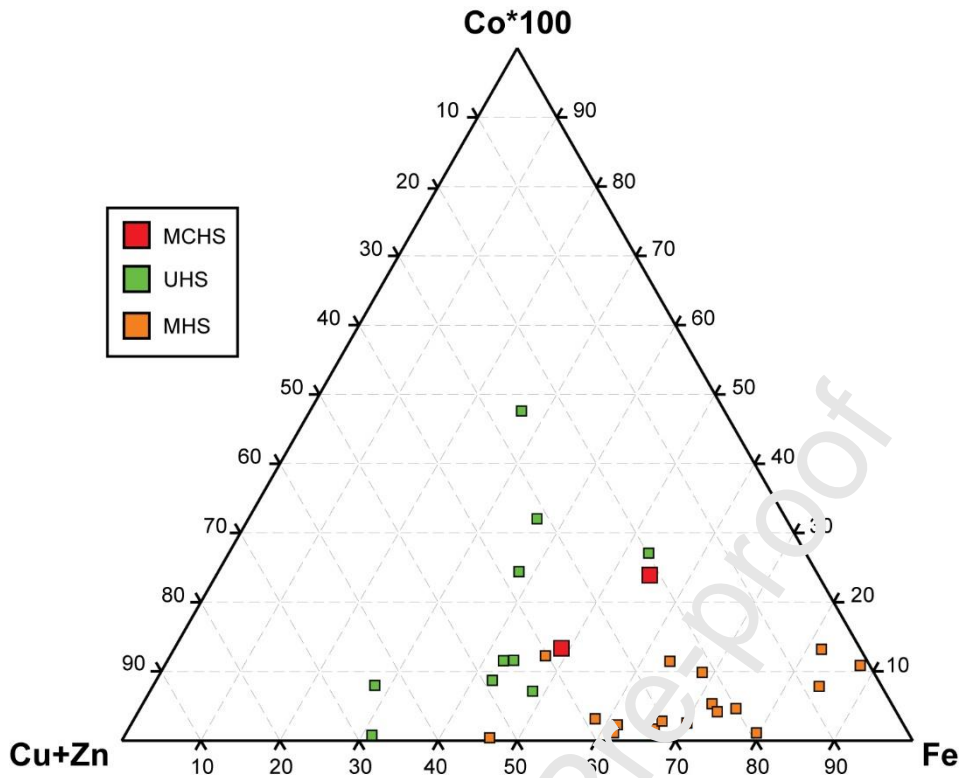


Figure 4. Ternary diagram of normalized metal composition of the Cu-rich Massive Sulfides facies at the MCHS compared to present-day Seafloor Massive Sulfides (from Fouquet et al., 2010).

## 4.2. Vertical distribution of elements

### 4.2.1. Whole rock

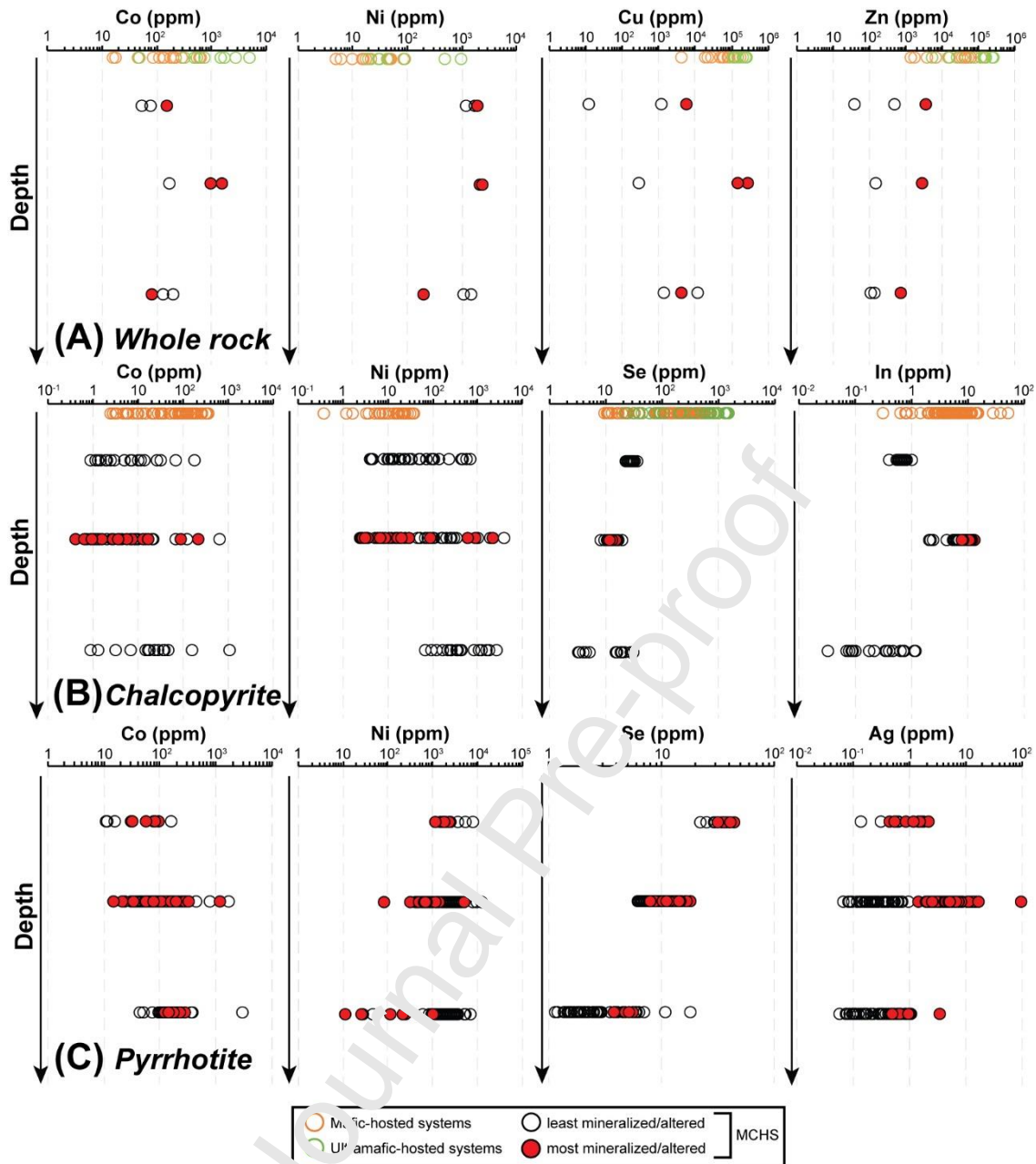


Figure 5. Vertical distribution of selected trace (A) elements in whole rocks and trace element in chalcopyrite (B) and pyrrhotite (C). At a given depth, the most mineralized/altered samples are displayed in red. All distributions are compared to values of present-day seafloor massive sulfides at mafic- and ultramafic-hosted systems (when available in the literature). (from Fouquet et al., 2010 and references therein; Wohlgemuth-Ueberwasser et al., 2015; Melekestseva et al., 2017; Grant et al., 2018; Yuan et al., 2018)

Whole rock compositions are marked by an increase of the CaO together with the Sr content (table 1) at Snake Pit, likely in relation to carbonation. MgO and MnO are also enriched there,

whereas  $\text{Fe}_2\text{O}_3$  is depleted. Trace elements (figure 5A) do not display specific evolution upwards.

Noticeably, the Ni content of mineralized rocks at the MCHS is higher than the one of present-day SMS either in mafic- or ultramafic-hosted systems, whereas the Co contents are comparable (Fouquet et al., 2010). As a consequence, the Co/Ni ratio of whole rocks at the MCHS is lower than the one of present-day massive sulfides (figure 6), the lowest values being recorded at Snake Pit. At a given structural level, the highest Co/Ni ratio is recorded in the most altered and/or mineralized samples (figure 6). It seems that this ratio decreases upwards at the MCHS (figure 6). Zn is depleted at the MCHS compared to present-day systems. Finally, the highest Cu contents of the MCHS are recorded at Marmorera section and are comparable to present-day seafloor massive sulfides.

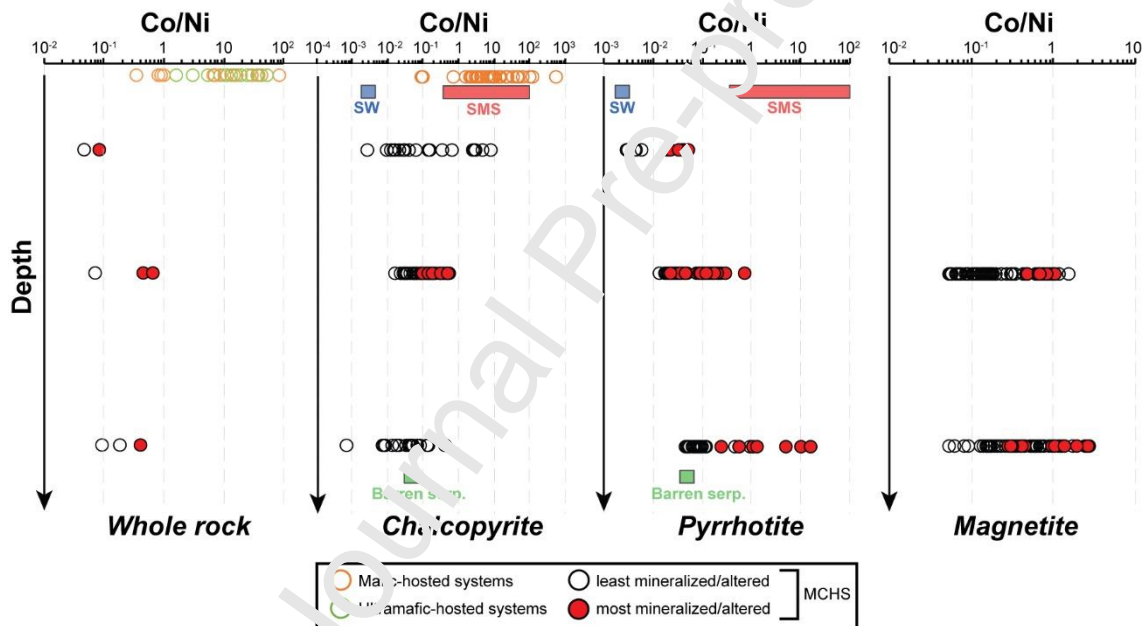


Figure 6. Co/Ni ratio of whole rocks and metal-bearing phases (chalcopyrite, pyrrhotite and magnetite) from the MCHS compared to present-day Seafloor Massive Sulfides and chalcopyrite (there is no LA-ICPMS data in the literature for pyrrhotite and magnetite). At a given depth, the most mineralized/alterated samples are displayed in red. The Co/Ni ratio of barren serpentinites (Barren serp., green square), seawater (SW, blue square) and seafloor massive sulfides (SMS, red boxes) are plotted. The Co/Ni ratio of barren serpentinites ( $\sim 0.05$ ) is averaged from chemical compositions of worldwide serpentinites in the literature consistently with the one measured in the barren serpentinite analyzed in this study. The Co/Ni ratio for seawater is from Sohrin et al. (1998). Note that the two lowest Co/Ni ratios measured in present-day chalcopyrite are the ones of minerals from the stockwork beneath

the TAG hydrothermal mound. Whole rocks and single grain chemical data from Fouquet *et al.*, 2010 and references therein; Melekestseva *et al.*, 2017; Grant *et al.*, 2018; Yuan *et al.*, 2018.

## 4.2.2. Minerals

### 4.2.2.1. Chalcopyrite

In chalcopyrite, Ni and Te concentrations decrease upwards (Te is below the limits of detection at Snake Pit) and Se concentrations increase (figure 5B). Chalcopyrite from SMS extends these trends for Ni and Se displaying low Ni and high Se concentrations ( $10^{-1}$  to  $10^2$  ppm and  $10^1$  to  $10^3$  ppm, respectively). On the other hand, chalcopyrite from present-day SMS displays Te contents one to two orders of magnitude higher than those of the MCHS (table 3). Indium does not display particular vertical distribution, with maximum In concentration at Marmorera (up to 13ppm) being comparable to present-day systems (figure 5B). Cobalt concentrations overlap along the section (figure 5B). The Co/Ni ratio spans a wide range, especially at Snake Pit (from  $10^{-3}$  to  $10^1$ , figure 6) and describes a funnel-like evolution. At Cotschen, the Co/Ni ratio is close to the one of barren serpentinite (0.05) whereas at Snake Pit the Co/Ni ratio spans between the ones of seawater (0.0025) and chalcopyrite from SMS (~ from  $10^0$  to  $10^3$ ). At Marmorera, the highest Co/Ni ratio is measured in the most mineralized sample (i.e. in the Cu-rich massive sulfides facies).

### 4.2.2.2. Pyrrhotite

In pyrrhotite (figure 5C), the Sn content increases upwards similarly to chalcopyrite (figure 5B), from 1 to 18 ppm at Cotschen to 22 to 44 ppm at Snake Pit. A slight increase of the Ge content occurs upwards (table 4). The maximum of the Ag content is recorded in Cu-rich MS from Marmorera (up to 97 ppm).

Nickel concentrations increase upwards (from  $10^1$  to  $10^4$  ppm at Cotschen to  $10^3$  to  $10^4$  ppm at Snake Pit) whereas Co decreases upwards. As a result, the Co/Ni ratio decreases regularly upwards and get close to the value of seawater (figure 6). Realistically, the Co/Ni ratio in pyrrhotite is between the ones of seawater, barren serpentinites and present-day seafloor massive sulfides (figure 6). The highest Co/Ni ratios are measured in the most mineralized/altered samples at a given depth similarly to what is measured in chalcopyrite (figure 6).

### 4.2.2.3. Magnetite

Magnetite has been only observed at Cotschen and Marmorera (figure 2C). A slight increase of Co, Ni, V and Ti concentrations is documented upwards (table 5). Mn concentrations are identical for the two sites. A large dispersion of trace elements in magnetite is the most prominent feature (table 5), likely in relation with the different textural forms of magnetite identified from petrography (i.e. in veins or in the groundmass around spinel relics, figure 2C). Noticeably, the Co/Ni ratio of magnetite is highest in the most mineralized/altered facies both at Cotschen and Marmorera (figure 6), as it was documented for chalcopyrite and pyrrhotite.

### 4.3. Lateral distribution of elements at Marmorera

#### 4.3.1. Whole rock

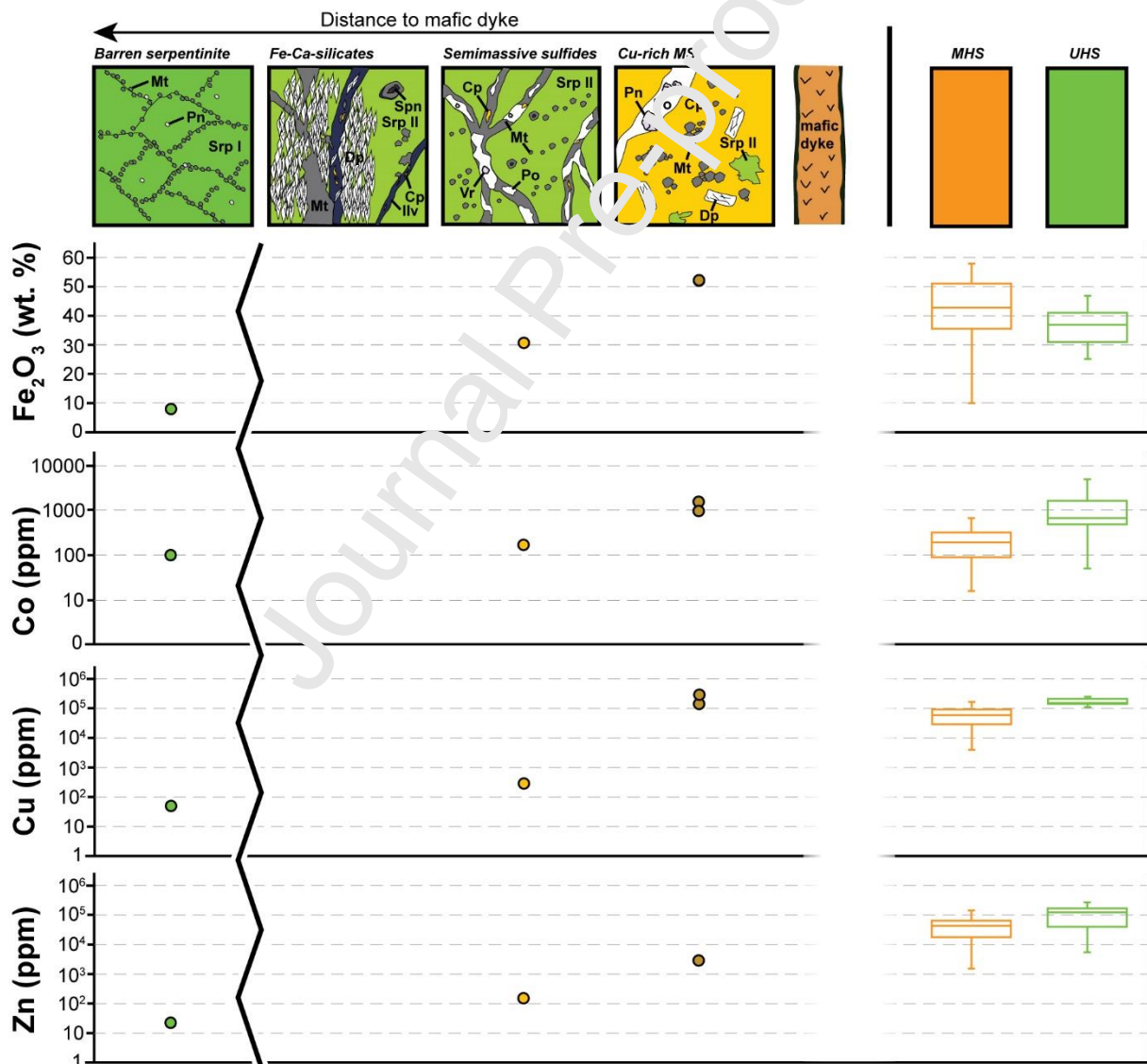


Figure 7. Major and trace element compositions of whole rocks of the Marmorera mineralized system. Data from present-day seafloor massive sulfides are reported as box

*plots for comparison (from Fouquet et al., 2010 and references therein). The boxplot is built as follow, in this figure and in the following, from the bottom to the top: minimum, first quartile, median, third quartile, maximum values. MHS=Volcanic-Hosted Systems, UHS=Ultramafic-Hosted Systems.*

Major and trace element of Marmorera samples are displayed in figure 7. Towards the mafic dyke, the  $\text{Fe}_2\text{O}_3$  content increases whereas the  $\text{SiO}_2$  and  $\text{MgO}$  contents decrease (tables 1, 2). These evolutions are consistent with the replacement of former serpentine by metal-bearing phases (figure 2C). CaO is slightly enriched in one sample of the Cu-rich MS facies where it is hosted by metasomatic diopside.

Progressive enrichments of Co, Cu and Zn are recorded towards the mafic dyke (figure 7). In the Cu-rich MS facies, the Co and Cu contents are close to those measured in present-day seafloor massive sulfides, whereas the Zn content is one to two orders of magnitude lower. The Ni concentrations are roughly constant at Marmorera (~2200 ppm) and are one to three orders of magnitude higher than in present-day seafloor massive sulfides (tables 1, 2). The Co/Ni ratio of the whole rocks (figure 8) displays a well-defined increase towards the mafic dyke, where it reaches values comparable to the lowest ones measured at present-day seafloor massive sulfides.

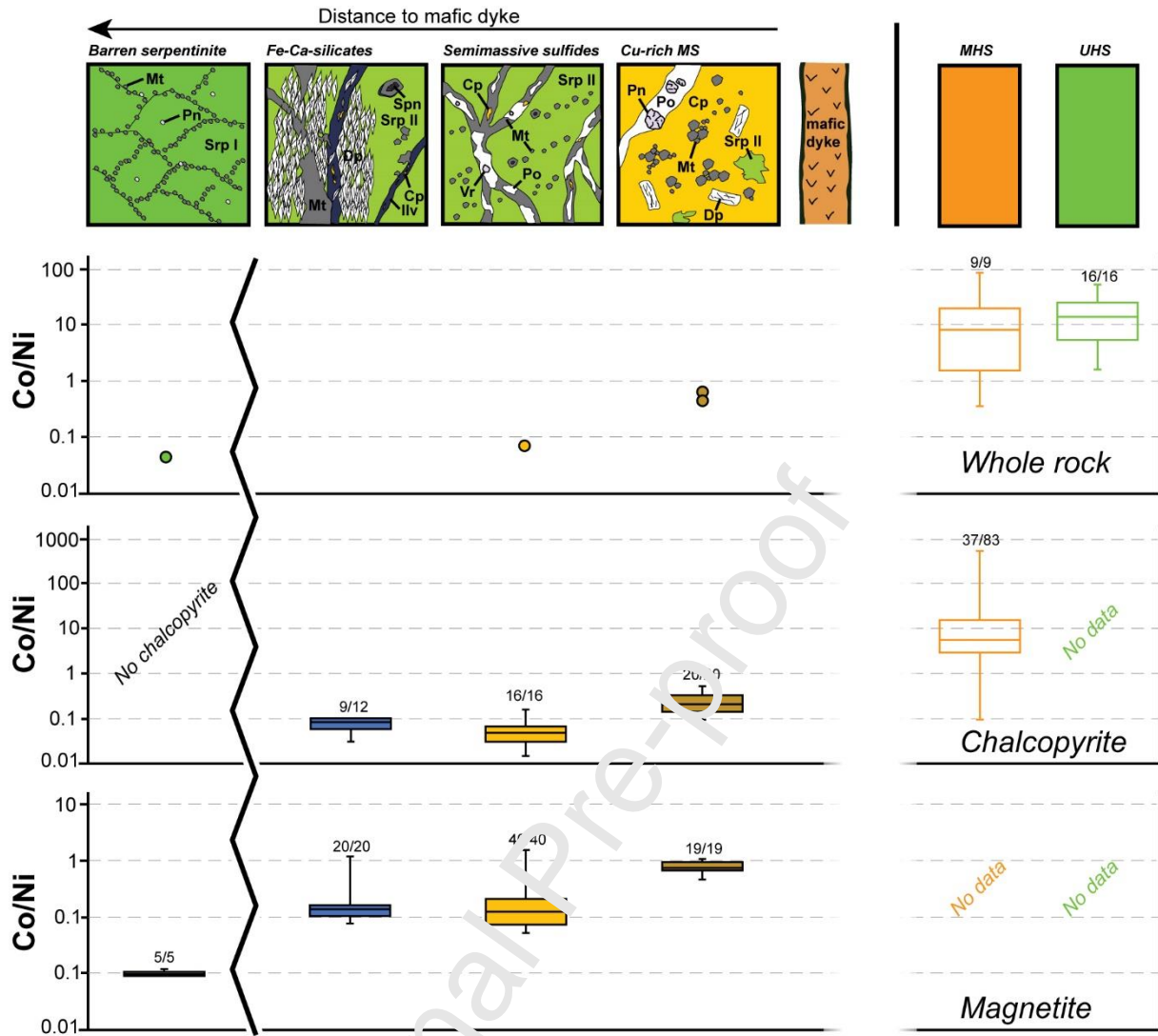


Figure 8. Co/Ni ratio variation in barren serpentinites, mineralized facies and hydrothermal phases of the Marmorera mineralized system. SMS and chalcopyrite from present-day systems are displayed for comparison (from Fouquet et al., 2010 and references therein; Melekestseva et al., 2017; Grant et al., 2018; Yuan et al., 2018). No LA-ICPMS Co contents available for magnetite. The ratio displayed above the boxplots indicates the number of values above the limits of detection against the number of analyses.

#### 4.3.2. Minerals

##### 4.3.2.1. Chalcopyrite

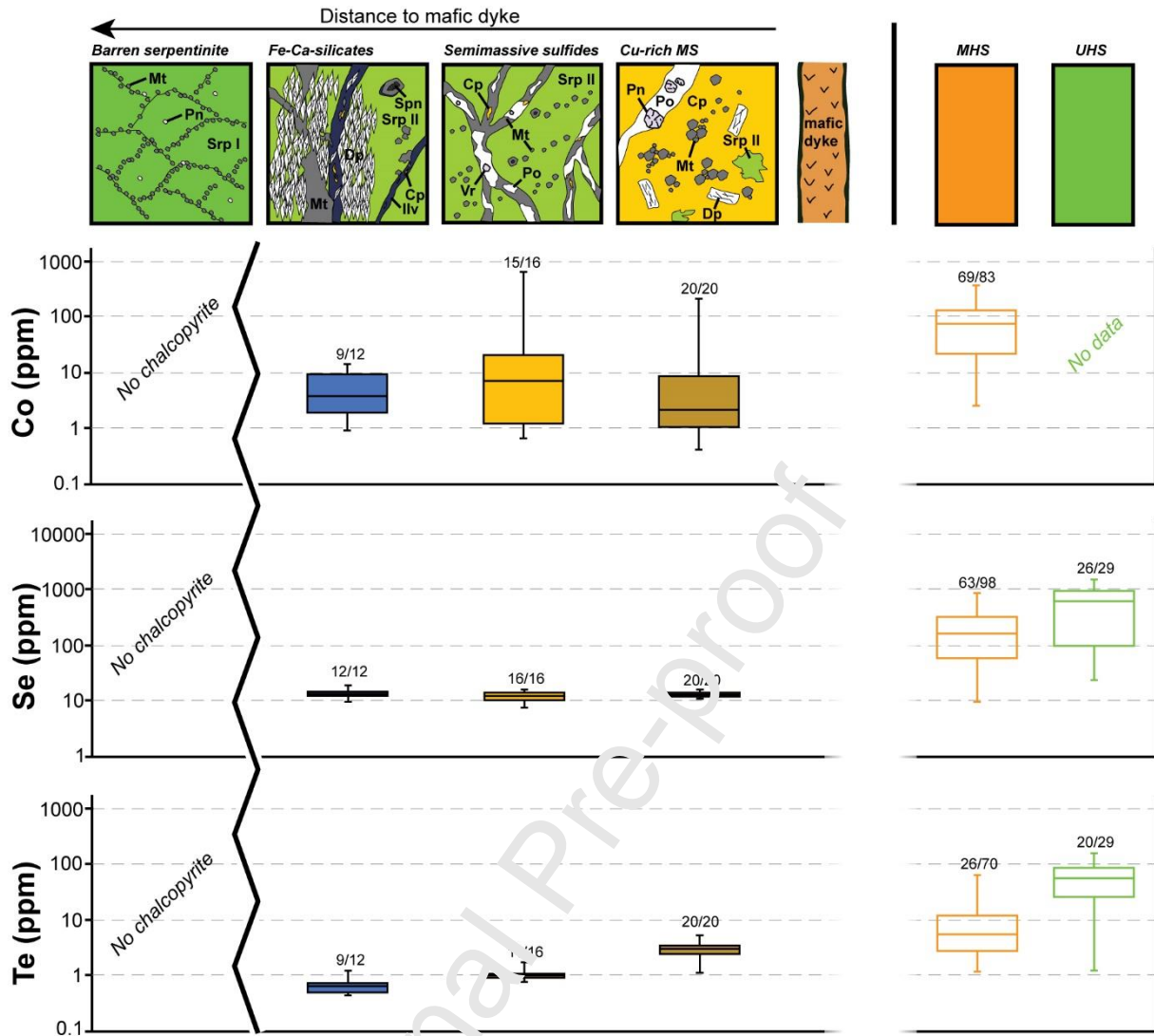


Figure 9. Concentrations of selected trace elements in chalcopyrite of the Marmorera mineralized system. Chalcopyrite from present-day hydrothermal systems are reported for comparison (data from Wohlgemuth-Ueberwasser et al., 2015; Melekestseva et al., 2017; Grant et al., 2018; Yuan et al., 2018).

In chalcopyrite (figure 9), the Co content is variable along the section without clear evolution towards the mafic dyke. The same evolution is recorded for the Ni content (table 3). The Ni content in the Cu-rich MS facies is close to the one of present-day systems, whereas the Co content is one to two orders of magnitude lower than present-day systems (table 3, figure 9). The Ni content appears slightly lower in the Cu-rich MS facies compared to other hydrothermal facies (table 3). At first sight, the Co/Ni ratio of chalcopyrite slightly increases towards the mafic dyke reaching values comparable to the lower ones of chalcopyrite from present-day systems (figure 8).

The Se content is constant along the profile. In present-day systems, Se content of chalcopyrite is one to two orders of magnitude higher than at Marmorera (figure 9). The Te content increases progressively towards the mafic dyke.

#### **4.3.2.2. Pyrrhotite**

In pyrrhotite Co is slightly enriched in the Cu-rich MS facies compared to the semimassive sulfides facies, whereas Ni strongly decreases (table 4). This leaves a Co/Ni ratio which increases towards the mafic dyke (figure 8).

Selenium slightly increases towards the mafic dyke, whereas Ge slightly decreases. Finally, Ag strongly increases in Cu-rich MS compared to semimassive sulfides with a median around 0.24 and 5, respectively.

#### **4.3.2.3. Magnetite**

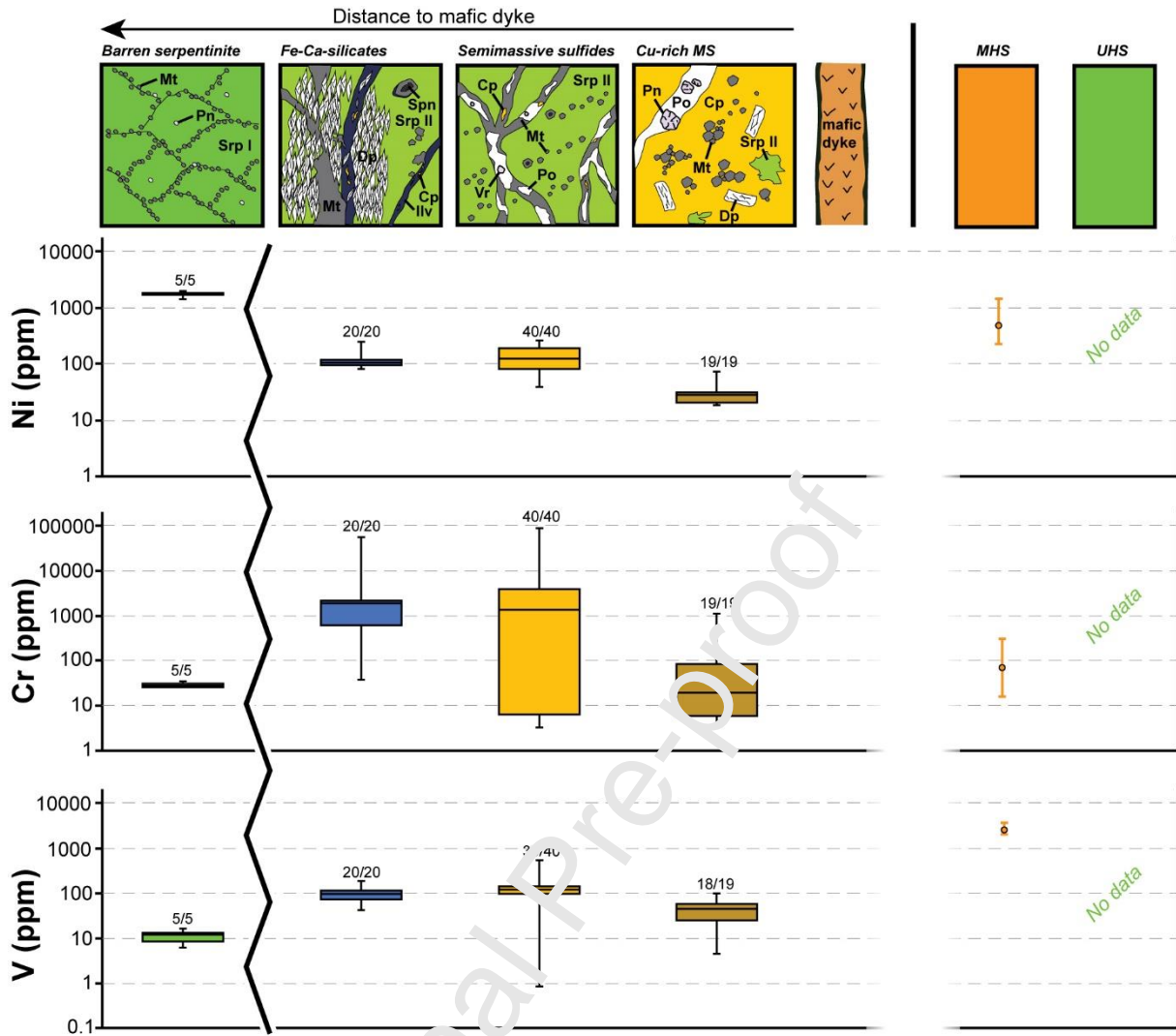


Figure 10. Concentrations of selected trace elements in magnetite of the Marmorera mineralized system. Magnetite from present-day systems are reported for comparison (data from Patten et al., 2016)

In magnetite (figure 10), Ni decreases towards the mafic dyke as it was observed for pyrrhotite and to a lesser extent for chalcopyrite (figure 9). The Co content is rather constant along the profile even if a slight increase may be noticed in the Cu-rich MS facies (table 5). As a consequence, the Co/Ni ratio increases in magnetite towards the mafic dyke (figure 8). V, Cr and Ti do not display a clear evolution towards the mafic dyke (table 5, figure 10). Barren serpentinites display somewhat lower V contents than their mineralized equivalents. Also, the semi-massive sulfides are characterized by a large dispersion of contents in Cr, V and Ti (table 5, figure 10).

In figure 11, we describe in more details the composition of magnetite, in relation with its textural position in the semimassive sulfides facies.

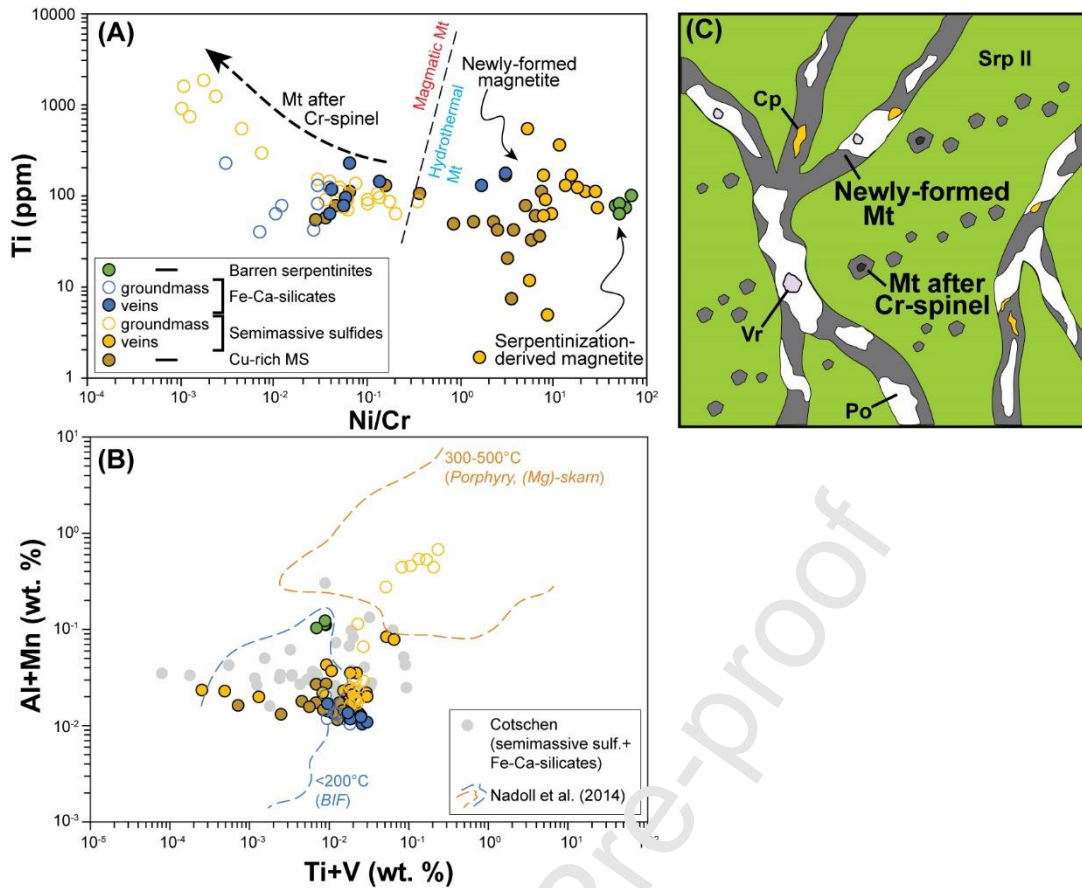


Figure 11. (A) Ti vs. Ni/Cr discriminant diagram of trace element compositions of magnetite from the Marmorera mineralized system (from Dare et al., 2014). Note that the field defined for magmatic and hydrothermal magnetite is displayed although it is rather discriminant for higher Ti concentrations. (B) Al+Min vs. Ti+V discriminant diagram of trace element compositions of magnetite from the Marmorera and Cotschen mineralized system (from Nadoll et al., 2014). (C) Schematic of the semimassive sulfides facies at Marmorera in which magnetite occurs either around former spinel or together with pyrrhotite in veins. Mt=magnetite, Cp=chalcopyrite, Po=pyrrhotite, Vr=violarite, SrpII=serpentine.

Magnetite in barren serpentinites displays the highest Ni/Cr ratio of about 60. Magnetite of the Fe-Ca-silicates and semimassive sulfides facies can be either found in the groundmass or in veins (figure 11C). In general, magnetite in the groundmass displays higher Ti content and lower Ni/Cr ratio than the one of veins (figure 11A). This is especially clear for magnetite of the semimassive sulfides facies. In the Cu-rich MS facies, magnetite displays variable Ti contents and Ni/Cr ratios overlapping those of semimassive sulfides and Fe-Ca-silicates facies. Unfortunately, the petrographic analysis did not allow to specify the textural features of magnetite in the Cu-rich MS facies.

In figure 11B, magnetite from the MCHS are widespread, covering both the field of low-T magnetite (from BIF deposits, Nadoll et al., 2014) and high-T magnetite (from porphyry and skarns deposits, Nadoll et al., 2014). A clear relationship between a hydrothermal facies and a given formation temperature is ambiguous. Rather, geochemical signatures of magnetite in the semimassive sulfide plot both in the low-T and high-T fields (figure 11B) precluding a straightforward of these signatures.

#### 4.4. Carbonated rocks at Snake Pit

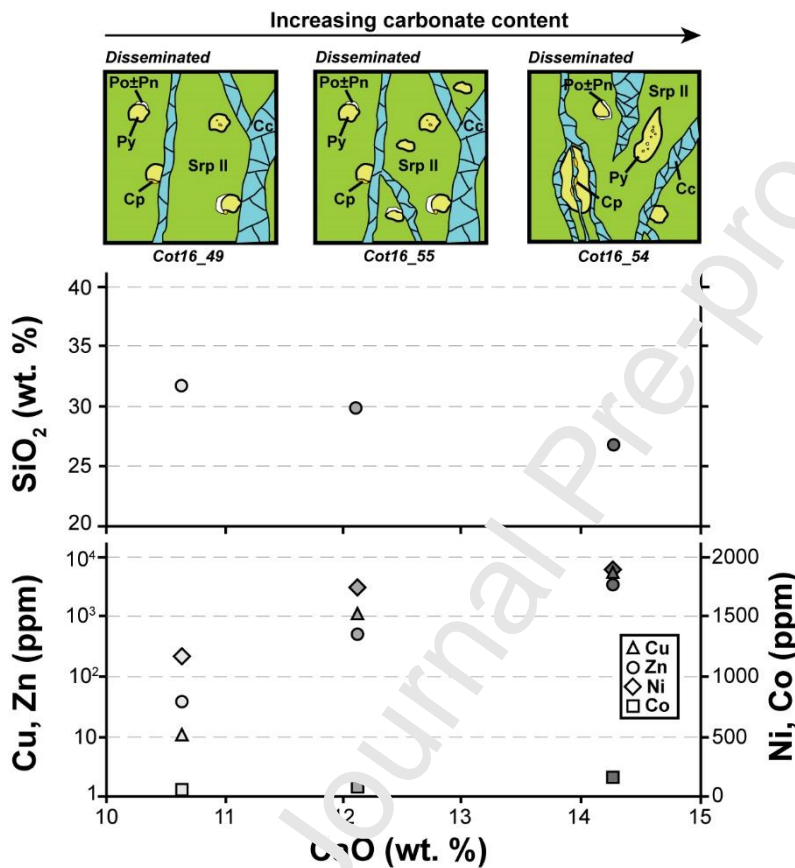


Figure 12. Concentrations of selected major and trace element in ophicalcites displaying variable degree of carbonation at Snake Pit.

At Snake Pit, the mineralized serpentinites are variably carbonated (figure 12). The CaO content is consistently variable (between 10.6 and 14.3 wt. %). The SiO<sub>2</sub> content (from 31.7 to 26.8 wt. %) is anticorrelated with CaO.

Copper and zinc increase by two orders of magnitude with CaO. This is consistent with the higher content of chalcopyrite and sphalerite in this sample. Cobalt and nickel slightly increase.

## 5. Discussion

### 5.1. A hydrothermal origin for the MCHS

Mineralization associated with ultramafic rocks are ascribed either to hydrothermal processes (similar to present-day ultramafic-hosted black smokers) or to magmatic activity (e.g. ortho-magmatic Ti-V-rich oxides deposits and Cu-Ni-rich sulfides linked to mafic or ultramafic intrusions). Here we have several petrographic and geochemical evidences which show that the mineralization formed in hydrothermal conditions.

The replacement of the serpentinite by the metal-bearing phases is a textural feature arguing for a hydrothermal origin for the mineralization. Coltat et al. (2019b) reported that the former lizardite is replaced by Fe-antigorite/greenalite where the mineralization occurs suggesting a metasomatic transformation during the fluid circulation.

Additionally, in magnetite, the low Ti contents coupled to quite high Ni/Cr (figure 11A) agree with a hydrothermal source rather than a magmatic one (Dare et al., 2014). The low Ni/Cr measured in magnetite in the groundmass are likely due to their presence around former spinel grains (figure 11B), the latter may contain high Cr and Ti contents. Dissolution-reprecipitation processes have likely enriched the newly formed magnetite in Ti and Cr, lowering the Ni/Cr ratio.

At the MCHS, the mineralization is depleted in Pt (it was only detected in few pyrrhotite, ~10%, appendix 2), an element characteristic of ortho-magmatic mineralized systems within mafic or ultramafic intrusions (Song et al., 2003). This depletion, hence, is also consistent with a hydrothermal origin for the mineralization.

### 5.2. Geochemical records of the variable Fluid/Rock ratio: the profile of Marmorera

The profile of Marmorera allows discussing the evolution of the Fluid/Rock (F/R) ratio during hydrothermal alteration, mainly for two reasons. First, the mineralization is geometrically controlled, here, by a mafic dyke. Secondly, the mineralization found here (figure 2B) displays the various end-members as a function of the intensity of the hydrothermal alteration at the MCHS (from the barren serpentinites to the Cu-rich MS).

At first order, the rocks close to the mafic dyke are more mineralized than those away from the mafic dyke suggesting that the F/R ratio increased towards the mafic dyke. This increase of the F/R ratio likely occurred during a single hydrothermal event, being free of any refining process. Indeed, there is no textural evidence of a previous mineralized assemblage preserved in the Cu-rich MS facies for example.

During the hydrothermal alteration, a decrease of the  $\text{SiO}_2$  and  $\text{MgO}$  content of the rocks and a gain of metals (Cu, Fe, Co, Zn) are observed. The metal content in the Cu-rich MS facies is comparable to the one reported at present-day SMS (figures 5, 6, 8, table 2) where the F/R ratio is obviously high. Noteworthy is that the Ni content remains fairly constant, so that the Co/Ni ratio of the mineralization was increased towards the dyke. Such an increase of the Co/Ni ratio together with the intensity of hydrothermal alteration has been previously reported in UHS (Marques et al., 2006; Fouquet et al., 2010) and in fossil VMS (Toffolo et al., 2017; Coltat et al., 2019b). The low Co/Ni ratios reported at the MCHS ( $<1$ ) are similar to the ones of deeply mineralized/altered rocks below ultramafic-hosted hydrothermal systems (Marques et al., 2007). This is consistent with the progressive replacement of serpentinite by hydrothermal phases rather than direct precipitation from the hydrothermal fluid (Fouquet et al., 2010). As a whole, the geochemical variations along the Marmorera profile are thus consistent with an increase of the F/R ratio towards the dyke, from of about 0 in the barren serpentinites to high values in the Cu-rich MS facies where fluids likely buffer the chemical composition of the mineralization. By extension, we propose that the internal geochemical variability observed at the two other investigated depths (Cotschen and Snake Pit) of the MCHS may be also explained by variable F/R ratios. Indeed, the most mineralized samples (red dots in figures 5 and 6) generally display the highest metal content and Co/Ni ratio and the lowest  $\text{SiO}_2$  and  $\text{MgO}$  contents.

### 5.3. Vertical evolution of chemico-physical parameters of the F-R interactions.

The whole range of some geochemical markers along the vertical section plots out the range measured at Marmorera (the site where F/R ratios are the largest). These are for example the Se content and the Co/Ni ratio. The Se content increases both in pyrrhotite and chalcopyrite upwards precluding a potential partitioning solely explained by a coefficient partition between the two sulfides. To explain the apparent upwards increase of the Se content and the lowering of the Co/Ni ratio we have thus to invoke chemico-physical parameters of fluid-rock interactions other than F/R ratio variations, that evolved along the vertical section. Like in present-day oceanic hydrothermal systems below black smokers, one may expect variations of pressure, temperature, pH and changes of  $f_{\text{O}_2}$  and  $f_{\text{S}_2}$ .

*Pressure.* At the MCHS, the lithostatic pressure decreased from the bottom of the system towards Snake Pit simply because Snake Pt is closer to the detachment (and to the paleo-

seafloor) than Cotschen. The decrease of the pressure has no strong influence on the solubility of hydrothermal phases (Reed and Palandri, 2006). In addition, mineralogical assemblages reported at present-day UHS and MHS are comparable to those at the MCHS suggesting pressure had no strong control on the mineralogy (even if one considers a slightly different water column depth). Therefore, the pressure decrease is unlikely to explain the variation of the geochemical markers upwards.

*Temperature.* The temperature is a key parameter controlling solubility or precipitation of metals in hydrothermal fluids (Reed, 1983). The presence of Fe-Ca-silicates associated with the mineralization at the deepest structural position of the MCHS indicates temperature of about  $425\pm 75^{\circ}\text{C}$  (Gustafson, 1974; Coltat et al., 2019b). The vanishing of Fe-Ca-silicates at Snake Pit may thus likely reflect a decrease of the temperature upwards. Also, at Snake Pit, the mineralization is mainly comprised of pyrite against pyrrhotite, a feature consistent with a potential slight temperature decrease and changes of redox and  $f_{\text{S}_2}$  (Hannington et al., 1995). Ni is rather immobile in low-T fluids ( $<400^{\circ}\text{C}$ ) whereas Co is mobile in fluids at lower temperatures, what is inferred by the presence of Co-rich minerals in both low-T and high-T chimneys at present-day systems (Fouquet et al., 2010). This may explain the lack of Ni enrichment or depletion of the mineralized rocks upwards and the slight decrease of Co at Snake Pit (figure 5), leaving an apparent decrease of the Co/Ni ratio at Snake Pit (figure 6). The present-day systems extend these variations, being rather poor in Ni (few nickel has been transported towards the seafloor) and rather rich in Co (figure 5). The decrease of the Co/Ni ratio observed upwards (figure 5) could be thus, at least partly the sign of a temperature decrease.

Selenium solubility has been poorly investigated, using thermodynamic modelling, at temperatures higher than  $300^{\circ}\text{C}$  (Huston et al., 1995; Xiong et al., 2003) which may likely be considered in the root zone of hydrothermal systems. Most of metals have solubility which decreases with temperature (Reed and Palandri, 2006), thus one may expect that the same effect would prevail for Se. Also, it may be envisaged that a temperature decrease of the hydrothermal fluid would have only lowered the solubility of Se complexes and precipitated Se in sulfides.

*pH.* Drastic pH changes are expected to occur during the uprising of hydrothermal fluid and mixing with seawater (Reed and Palandri, 2006). Generally, HT hydrothermal fluids in ultramafic settings are highly acidic (Charlou et al., 2002; Tivey, 2007) whereas seawater is

slightly basic pH (7.8). The mixing between these two fluids causes abrupt pH changes, destabilizing the metal complexes carried in the hydrothermal fluids and ending with metal deposition. Se is more efficiently mobilizable under acidic conditions (Huston et al., 1995) explaining its presence in typical hydrothermal fluids. Hence, a rapid increase of the pH would lead to Se precipitation from the hydrothermal fluid, a scenario supported by the highest Se content measured in metal-bearing phases from the upper part of the system, which is consistent with a progressive mixing between the hydrothermal fluid and seawater.

$f_{O_2}$ ,  $f_{S_2}$ . The oxygen and sulfur fugacity are highly modified in hydrothermal systems during the mixing of the hydrothermal fluid with seawater. The pyrite-pyrrhotite-magnetite assemblage represent a buffer both for  $f_{O_2}$  and  $f_{S_2}$  (Hannington et al., 1995). The presence of magnetite and pyrrhotite at apparent textural equilibrium at Cotschen and Marmorera indicates medium  $f_{O_2}$  and low  $f_{S_2}$ . At Snake Pit, the apparition of pyrite, as the main metal-bearing phase, and the absence of magnetite both suggest an increase of the  $f_{S_2}$  and possibly  $f_{O_2}$  at very high  $f_{S_2}$  (Hannington et al., 1995).

Selenium is more efficiently carried by oxidized fluids rather reduced ones and is more easily transported under medium ( $\sim 150^\circ\text{C}$ ) rather than hot ( $\sim 300^\circ\text{C}$ ) conditions (Huston et al., 1995). At HT ( $300^\circ\text{C}$ ), in the stability field of pyrite (agreeing with the mineralogy reported at Snake pit), Se is transported under its reduced form  $\text{H}_2\text{Se}$  (Xiong et al., 2003). This indicates that while an overall oxidation of the system would occurred, it remained reduced enough to prevent modification of the Se speciation in the hydrothermal fluid. Also, Se is expected to be more enriched in fluid under the conditions where pyrite is stable. Hence, one would expect that oxidation of the hydrothermal fluid would enhance Se leaching from the basement rocks but would keep Se into the hydrothermal fluid. This should have decreased the Se content in sulfides formed at Snake pit, a reverse trend than the one reported. An oxidation of the hydrothermal fluid upwards, therefore does not entirely satisfy the apparent increase of the Se content in sulfides.

#### **5.4. Model of circulation: mixing with seawater during upwards hydrothermal circulation**

The increase of the Se content in chalcopyrite and pyrrhotite and the decrease of the Co/Ni ratio upwards indicate variations of the temperature, pH,  $f_{O_2}$  and  $f_{S_2}$  in the hydrothermal system. A simple model of progressive decrease of the temperature and/or increase of the  $f_{O_2}$  of the hydrothermal fluid does not allow to reconcile neither the evolution of these

geochemical markers nor the observed mineralogical assemblages. So, we propose a model of fluid mixing to explain the geochemical and mineralogical variations observed at the MCHS (figure 14). In this model, HT hydrothermal fluids mixed with seawater as it flew upwards. The seawater percolated in the host serpentinites, and likely moved towards the main hydrothermal channel flow as a result of small-scale circulation paths.

The Co/Ni ratio of the mineralized rocks is between those of barren serpentinites (0.05) and seawater (0.0025). The seawater activity is maximal at Snake Pit where the lowest Co/Ni ratios are reported, what is intuitive as Snake Pit is closer to the detachment than Cotschen. The progressive mixing between the HT hydrothermal fluid and seawater is likely responsible for the decrease of the temperature and the increase of the  $f_{O_2}$ .

A seawater-derived fluid was more oxidized than the uprising hydrothermal fluid. In addition, this fluid may represent an additional source for Se. The mixing between these two fluids was likely efficient to destabilize  $H_2Se$  complexes during sulfide formation and to enrich Se in sulfides. This leaves the Se increase in the mineralization upwards (figure 5). However, we cannot preclude that part of the Se enrichment upwards was only due to the temperature decrease of the hydrothermal fluid. A combination of the two processes (i.e. temperature decrease and mixing with seawater) is thus proposed to explain the increase of the Se content in sulfides upwards.

The high contents of Mn and Mo (table 3) of chalcopyrite at Snake Pit agree with a lowering of the temperature partly due to the mixing with seawater. In present-day hydrothermal systems, Mn is found in oxyhydroxides formed at the outer part of hydrothermal systems (Fouquet et al., 2010) where temperature is low (< 30°C) and oxidation conditions favor its precipitation. The increase of the MnO content in rocks at Snake Pit is thus consistent with an overall oxidation of the system during the mixing with seawater even if still low oxygen fugacity prevented the formation of Mn-rich phases.

Even if a hydrothermal model implying mixing between the hydrothermal fluid with seawater allows to explain the upwards variation of the geochemical markers, we cannot discard that a potential late refining occurred at Snake Pit. This refining could have been linked to the hydrothermal conditions that end up with carbonation. This hypothesis is consistent with the increase of the metal content together with the carbonation rate (figure 12) and could be the consequence of the MnO increase in mineralized rocks (figure 5) at Snake Pit. In that case, medium fluids (~130°C) would have remobilized a part of the former metal stock. The presence of chalcopyrite together with calcite filling cracks into pyrite grains and aggregates

at Snake Pit likely indicates that a slight part of the Cu stock has been remobilized during carbonation. However, it does not explain the high contents of Zn, Co and Ni notably because that we have no textural evidence for late enrichment of these elements. Another hypothesis is then that the most carbonated sample at Snake Pit was fortuitously the most mineralized during the former hydrothermal stage. Only an extensive sampling set could allow specifying this point.

In the figure 13, the exact pathway of fluids is speculative. The fluids may have used the detachment plane itself as a channel or percolate through fractures in the serpentinite basement. HT fluids might have derived from several sources or a combination of sources. These are i) modified seawater (i.e. reduced and acidic) which would have interacted with mafic intrusions and serpentinites at depth, ii) serpentinization reactions and iii) exsolution of magmatic fluids. These fluids get heated in-depth thanks to the cooling of magmatic intrusions where they leach metals from the basement rocks, presumably serpentinites and mafic rocks, similarly to what is proposed in present-day ultramafic-hosted systems (Marques et al., 2006). Also, it may be envisaged that seawater itself could have contributed to metal enrichment especially for Se. Further isotopic analyses (Sr isotope signatures of Fe-Ca-silicates accompanying the mineralization) would be useful to address this point. On the way back to the surface, the HT hydrothermal fluid is focalized along preferential pathways (like the contact between the dyke and the serpentinites at Marmorera) and progressively mixes upwards with seawater (with a lower temperature) that impregnated the host serpentinites. Where the F/R ratio increased (i.e. in area where the fluid flow was maximum), the Co/Ni ratio of the mineralization increased (figure 13B). This hydro-metallogenic model is consistent with the latest hydrothermal stage recorded at Snake Pit which is marked by a seawater-derived carbonation of mantle rocks (Coltat et al., 2019b). It also reconciles the mineralogical evolution observed at Snake Pit by an overall oxidation during the mineralizing event thanks to the influx of serpentinite-hosted seawater.

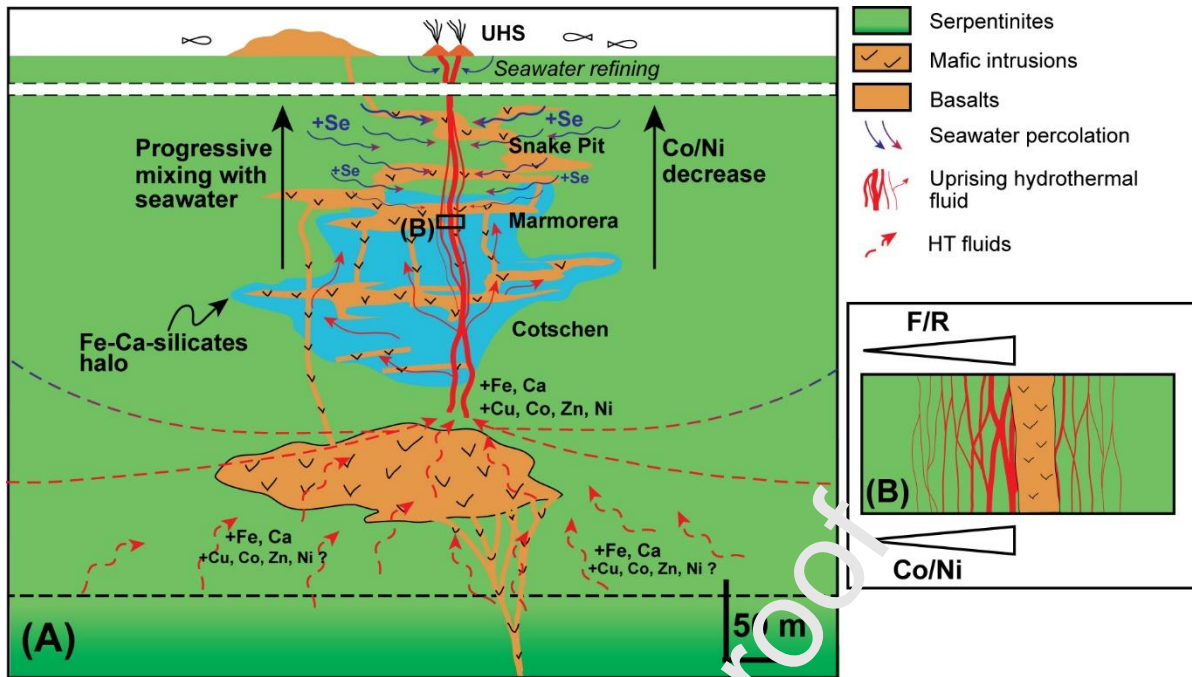


Figure 13. Hydrodynamic and metallogenic model for the formation of the mineralized system at the MCHS (the carbonation event occurred subsequently and is not displayed). The mineralization forms from the progressive mixing between the HT hydrothermal fluid and seawater upwards. The exact source for metals remains unknown. See text for details.

### 5.5. Insights for present-day black smoker deposits

The Co/Ni ratio of present-day mineralization at the seafloor is higher than the one of serpentinite (figure 3, 6). Along the MCHS vertical section, we have documented a decrease of this ratio at Snake Pit in response to a decrease of the temperature, conditions favorable for cobalt mobility and nickel precipitation. On the other hand, the fluid that interacted with the rocks should display a high Co/Ni ratio. When these fluids reach the seafloor, they undergo an abrupt chemical discharge, so that the mineralization records the characteristics of the fluid itself. The high Co/Ni of present-day systems thus likely represents the final product of the chromatographic evolution recorded along the MCHS section. Although we have no petrographic evidence (e.g. coeval precipitation of Ni and Co-rich sulfides with calcite), another process to explain the high Co/Ni ratio could relate to the remobilization of the Co stock during late carbonation without strong incidence on Ni. This would enrich the mineralization in Co relative to Ni and increase the Co/Ni ratio at Snake Pit.

The progressive increase of the Se content upwards recorded both in chalcopyrite and pyrrhotite is clear (figure 5). It is likely indicative that Se was more efficiently precipitated from the hydrothermal fluid in the upper parts of the section. Also, a part of Se would have

been brought by seawater. In present-day systems, Se is enriched in HT chimneys (rich in Cu) whereas LT chimneys (rich in Fe and Zn) are more depleted (Rouxel et al., 2004b). However, the Cu content of present-day SMS and Cu-rich MS at the MCHS is comparable but chalcopyrite in the latter is depleted in Se compared to present-day equivalents. This indicates that process other than only temperature-related would enrich the mineralization formed at the seafloor. Martin et al. (2018), based on geochemical signatures of the mineralization at Troodos, showed that Se enrichment from sulfide dissolution occurred during oxidation processes. It might be expected that similar processes occur at present-day SMS likely during the circulation of seawater-derived oxidized fluids interacting with the former mineralization. The high Se content of chalcopyrite measured in present-day mineralized systems (figure 5) could thus be the final stage of the evolution recorded along the MCHS section coupled to potential late refining processes and possible volatile magmatic additions (Keith et al., 2016; Melekestseva et al., 2017; Patten et al., 2020).

Zinc has unusually low concentration in the mineralization at the MCHS compared to present-day black smokers. It is unlikely due to different intensities of hydrothermal alteration since Cu, Fe and Co contents in Cu-rich MS are comparable to those of UHS and MHS. In the latter, Zn is enriched in low-T chimneys (Fouquet et al., 2010) suggesting that it is soluble at low temperatures in hydrothermal fluids (Reed and Palandri, 2006). Therefore, the depletion of Zn at the MCHS may be due to the high temperature of hydrothermal fluids in which Zn was still soluble and did not precipitate to form Zn sulfides. Nevertheless, the low Zn concentrations measured in the mineralization at the MCHS could also be the consequence of a low budget of mafic rocks available to extract Zn (mafic rocks are enriched in Zn with respect to ultramafic rocks, Fouquet et al., 2010).

Silver shares affinities with Zn in present-day mineralized systems where it is found in low-T sulfide chimneys (Fouquet et al., 2010). At the MCHS, the Cu-rich MS are slightly enriched in Ag (up to 119 ppm) compared to present-day mineralized systems. But the low Ag content at the MCHS with respect to UHS indicates that, similarly to Zn, Ag was not efficiently precipitated and was evacuated in the hydrothermal fluid towards the surface. Noteworthy is that in chalcopyrite at Marmorera (figure 9), the content of Ag increases in the most mineralized sample. This suggests that even in high-T mineralogical assemblages, Ag can be scavenged where the intensity of hydrothermal alteration increases.

Similarly, Ge shows geochemical affinities with Zn in UHS (Fouquet et al., 2010). Ge has been measured in pyrrhotite at the MCHS without apparent correlation to the intensity of

hydrothermal alteration, whereas Cu-rich MS are depleted in Ge. This may be explained by the solubility of Ge in hydrothermal fluids at the MCHS. As a consequence, it was likely transported together with Ag and Zn towards the surface.

Gold is an element locally enriched at ultramafic-hosted systems (Fouquet et al., 2010; Melekestseva et al., 2017; Webber et al., 2017; Knight et al., 2018). There, native or electrum gold co-precipitates with sulfides from the hydrothermal fluid in sulfides chimneys. At the MCHS, the mineralization is nearly Au-free; only a low Au content is reported in one sample of the Cu-rich MS facies (table 1). The lack of gold enrichment may be explained by two reasons: i) it was not extracted from the country rocks, ii) it was not trapped in the mineralization and was transported in hydrothermal fluids higher in the system. At the MCHS we do not know if the barren serpentinites are depleted in Au. However, at first order, there is no direct reason to preclude that Au was retained in the basement rocks during hydrothermal alteration at the MCHS. Its absence, hence, rather suggests that it was not incorporated in the mineralization. Au is mainly transported as chloride complexes in high-T acidic and oxidized hydrothermal fluids (Fouquet et al., 2010). The lack of Au in the mineralization suggests that the mixing between the hydrothermal fluid with minute proportions of seawater as it proposed for the MCHS (figure 13) was not efficient to destabilize the complexes and precipitate gold. A much more efficient trap is the arrival of the hydrothermal fluid at the seafloor, where seawater overwhelmingly dominates the mixing.

Finally, present-day seafloor massive sulfides may contain significant tellurium contents (Fouquet et al., 2010; Wohlgemuth-Ueberwasser et al., 2015). The position of Te in the element periodic table indicates that it shares similar geochemical behaviors with Se in hydrothermal fluids and is thought to be enriched in sulfides (Hertogen et al., 1980). This would explain why both Te and Se are found in present-day ultramafic-hosted systems. There, Te is sequestered in pyrite, whereas Se has more affinities with chalcopyrite (Rouxel et al., 2004b; Martin et al., 2020). At the MCHS, the Te content of the mineralization is lower than the one reported at UHS and Te does not show positive correlation to Se. We might thus suggest that Te is scavenged in pyrite at Snake Pit. The different Te content reported in chalcopyrite between the MCHS and UHS could be explained by processes similar to those controlling the Se enrichment at present-day settings.

## 6. Conclusion

The geochemical study of the Marmorera-Cotschen hydrothermal system brings insights on the element distribution occurring below present-day ultramafic-hosted mineralized systems. For the first time we report chemical signatures of metal-bearing phases and whole rocks equivalent to the root zone of present-day ultramafic-hosted hydrothermal systems. As a consequence, this study enhances to better understand element partitioning during metal deposition at depth. Hence, it allows to constrain hydrothermal processes which occur beneath active black smoker systems and are responsible for seafloor massive sulfides formation at the seafloor. The main conclusions of this study are as follows:

- (1) The upwards circulation of the mineralizing fluid was accompanied by a temperature decrease. This may have provoked a fractionation of the Co/Ni ratio.
- (2) The upwards mixing with seawater coming from the surrounding serpentinites was responsible for the increase of the  $f_{O_2}$  and Se content upwards.
- (3) The Co/Ni ratio evolves laterally as a proxy of the intensity of the fluid/rock interactions.
- (4) The temperature decrease upwards may as well be linked to the mixing with seawater coming from the serpentinites.
- (5) Late carbonation affecting the system was possibly responsible for minor metal remobilization. In present-day setting, it could be the cause of secondary low-grade deposits.

The Marmorera-Cotschen hydrothermal system should be considered further as a natural laboratory on which applying other tools, like isotope geochemistry, to better understand the processes acting at depth below black-smokers type hydrothermalism.

## Acknowledgments

The authors would like to thank S. McClenaghan in the Trinity College in Dublin for the help during the acquisition of LA-ICPMS data. A. Boissier and S. Cheron are thanked for the acquisition and processing of WD-XRF data. J. Langlade is acknowledged for the acquisition of EPMA analyses. This study was founded through CNRS-INSU-CESSUR and University of Rennes 1 “Défis Scientifiques” grants (accorded to P. Boulvais and R. Coltat).

## References

- Amann, M., Ulrich, M., Manatschal, G., Pelt, E., Epin, M.E., Autin, J., Sauter, D., 2020. Geochemical characteristics of basalts related to incipient oceanization: The example from the Alpine-Tethys OCTs. *Terra Nov.* 32, 75–88. <https://doi.org/10.1111/ter.12438>
- Andreani, M., Escartin, J., Delacour, A., Ildefonse, B., Godard, M., Dyment, J., Fallick, A.E., Fouquet, Y., 2014. Tectonic structure, lithology, and hydrothermal signature of the Rainbow massif (Mid-Atlantic Ridge 36°14'N). *Geochemistry, Geophys. Geosystems* 15, 3543–3571. <https://doi.org/10.1002/2014GC005269>. Received
- Beaulieu, S.E., Baker, E.T., German, C.R., Maffei, A., 2013. An authoritative global database for active submarine hydrothermal vent fields. *Geochemistry, Geophys. Geosystems* 14, 4892–4905. <https://doi.org/10.1002/2013GC004998>
- Candela, P.A., Wylie, A.G., Burke, T.M., 1989. Genesis of the ultramafic rock-associated Fe-Cu-Co-Zn-Ni deposits of the Sykesville District, Maryland Piedmont. *Econ. Geol.* 84, 663–675. <https://doi.org/10.2113/gsecongeo.84.3.663>
- Charlou, J.L., Donval, J.P., Fouquet, Y., Jean-baptiste, P., Holm, N., 2002. Geochemistry of high H<sub>2</sub> and CH<sub>4</sub> vent fluids issuing from ultramafic rocks at the Rainbow hydrothermal field (36°14'N, MAR). *Chem. Geol.* 191, 345–359.
- Coltat, R., Boulvais, P., Branquet, Y., Collot, J., Epin, M.E., Manatschal, G., 2019. Syntectonic carbonation during synmagmatic mantle exhumation at an ocean-continent transition. *Geology* 47, 183–186. <https://doi.org/10.1130/G45530.1>
- Coltat, R., Branquet, Y., Gautier, P., Campos Rodriguez, H., Poujol, M., Pelleter, E., McClenaghan, S., Manatschal, G., Boulvais, P., 2019. Unravelling the root zone of ultramafic-hosted black smokers-like hydrothermalism from an Alpine analog. *Terra Nov.* 31, 549–561. <https://doi.org/10.1111/ter.12427>
- Coltat, R., Branquet, Y., Gautier, P., Boulvais, P., Manatschal, G., *in rev.* The nature of the interface between basalts and serpentinized mantle in oceanic domains: insights from a geological section in the Alps. *Tectonophysics*.
- Dare, S.A.S., Barnes, S.-J., Beaudoin, G., Méric, J., Boutroy, E., Potvin-Doucet, C., 2014. Trace elements in magnetite as petrogenetic indicators. *Miner. Depos.* 49, 785–796. <https://doi.org/10.1007/s00126-014-0529-0>
- De la Roche, H., Marchal, M., 1978. Leucogranites et granites du massif de Valencia de Alcantara (Espagne): Relations entre compositions minéralogiques et faciès mineral. *Sci. la Terre* 22, 181–200.

Desmurs, L., Müntener, O., Manatschal, G., 2002. Onset of magmatic accretion within a magma-poor rifted margin: a case study from the Platta ocean-continent transition, eastern Switzerland. *Contrib. to Mineral. Petrol.* 144, 365–382. <https://doi.org/10.1007/s00410-002-0403-4>

Dietrich, V., 1972. Die sulfidischen Vererzungen in den Oberhalbsteiner Serpentiniten. *Geotech. Ser.* 49, 129.

Dietrich, V., 1970. Die Stratigraphie der Platta-Decke: facielle Zusammenhänge zwischen Oberpenninikum und Unterostalpin. *Eclogae Geol. Helv.* 63, 631–671.

Dunoyer de Segonzac, G., Bernoulli, D., 1976. Diagenese et metamorphisme des argiles dans le Rhetien Sud-alpin et Austro-alpin (Lombardie et Grisons). *Bull. la Société Géologique Fr.* S7-XVIII, 1283–1293. <https://doi.org/10.2113/gssgfbull.S7-XVIII.5.1283>

Epin, M., Manatschal, G., Amann, M., 2017. Defining diagnostic criteria to describe the role of rift inheritance in collisional orogens: the case of the Err-Platta nappes (Switzerland). *Swiss J. Geosci.* 110, 419–438. <https://doi.org/10.1007/s00015-017-0271-6>

Epin, M.E., Manatschal, G., Amann, M., Ribes, C., Clause, A., Guffon, T., Lescanne, M., 2019. Polyphase tectono-magmatic evolution during mantle exhumation in an ultra-distal, magma-poor rift domain: example of the fossil Platta ophiolite, SE Switzerland. *Int. J. Earth Sci.* 108, 2443–2467. <https://doi.org/10.1007/s00531-019-01772-0>

Etoubleau, J., Cambon, P., Fouquet, Y., Henry, K., Moal, S., 1996. Séparation des métaux nobles (Pt, Au) d'une matrice géologique par chromatographie d'échange d'ions et détermination par spectrométrie de fluorescence X. *Le J. Phys.* IV 06, 843–852. <https://doi.org/10.1051/jp4:1996481>

Ferreiro Mählin, R., 1995. Das Diagenese-Metamorphose-Muster von Vitrinitreflexion und Illit-"Kristallinität" in Mittelbünden und im Oberhalbstein, Teil 1: Bezüge zur Stockwerktektonik. *Schweizerische Mineral. und Petrogr. Mitteilungen* 75, 85–122. <https://doi.org/http://doi.org/10.5169/seals-57145> Nutzungsbedingungen

Foose, M.P., 1985. Setting of a Magmatic Sulfide Occurrence in a Dismembered Ophiolite, Southwestern Oregon, U.S. Geological Survey Bulletin 1626. *Contributions to the Geology of Mineral Deposits.*

Foose, M.P., Economou, M., Panayiotou, A., 1985. Compositional and mineralogic constraints on the genesis of ophiolite hosted nickel mineralization in the Pevkos Area, Limassol Forest, Cyprus. *Miner. Depos.* 20, 234–240.

Fouquet, Y., Cambon, P., Etoubleau, J., Charlou, J.L., Ondréas, H., Barriga, F.J.A.S., Cherkashov, G., Semkova, T., Poroshina, I., Bohn, M., Donval, J.P., Henry, K., Murphy, P.,

Rouxel, O., 2010. Geodiversity of Hydrothermal Processes Along the Mid-Atlantic Ridge and Ultramafic-Hosted Mineralization: A New Type of Oceanic Cu-Zn-Co-Au Volcanogenic Massive Sulfide Deposit. *Geophys. Monogr. Ser.* 188, 321–367.

Froitzheim, N., Manatschal, G., 1996. Kinematics of Jurassic rifting, mantle exhumation, and passive-margin formation in the Austroalpine and Penninic nappes (eastern Switzerland). *Geol. Soc. Am. Bull.* 108, 1120–1133.

Froitzheim, N., Schmid, S.M., Conti, P., 1994. Repeated change from crustal shortening to orogen-parallel extension in the Austroalpine units of Graubünden Graubünden. *Eclogae Geol. Helv.* 87, 559–612.

Grant, H.L.J., Hannington, M.D., Petersen, S., Frische, M., Fuchs, S.H., 2018. Constraints on the behavior of trace elements in the actively-forming TAG deposit, Mid-Atlantic Ridge, based on LA-ICP-MS analyses of pyrite. *Chem. Geol.* 498, 45–71. <https://doi.org/https://doi.org/10.1016/j.chemgeo.2018.08.019>

Gustafson, W.I., 1974. The Stability of Andradite, Hedenbergite, and Related Minerals in the System Ca-Fe-Si-O-H. *J. Petrol.* 15, 455–500.

Hannington, M.D., Jonasson, I.R., Erzig, P.M., Petersen, S., 1995. Physical and Chemical Processes of Seafloor Mineralization at Mid-Ocean Ridges. *Geophys. Monogr. Ser.* 91, 115–157.

Hertogen, J., Janssens, M.-J., Palme, H., 1980. Trace elements in ocean ridge basalt glasses: implications for fractionations during mantle evolution and petrogenesis. *Geochim. Cosmochim. Acta* 44, 2125–2143. [https://doi.org/https://doi.org/10.1016/0016-7037\(80\)90209-4](https://doi.org/https://doi.org/10.1016/0016-7037(80)90209-4)

Huston, D.L., Sie S.F., Suter, G.F., 1995. Selenium and its importance to the study of ore genesis: the theoretical basis and its application to volcanic-hosted massive sulfide deposits using PIXE analysis. *Nucl. Inst. Methods Phys. Res. B* 104, 476–480. [https://doi.org/10.1016/0168-583X\(95\)00462-9](https://doi.org/10.1016/0168-583X(95)00462-9)

Keith, M., Haase, K.M., Klemd, R., Krumm, S., Strauss, H., 2016. Systematic variations of trace element and sulfur isotope compositions in pyrite with stratigraphic depth in the Skouriotissa volcanic-hosted massive sulfide deposit, Troodos ophiolite, Cyprus. *Chem. Geol.* 423, 7–18. <https://doi.org/10.1016/j.chemgeo.2015.12.012>

Knight, R.D., Roberts, S., Webber, A.P., 2018. The influence of spreading rate, basement composition, fluid chemistry and chimney morphology on the formation of gold-rich SMS deposits at slow and ultraslow mid-ocean ridges. *Miner. Depos.* 53, 143–152. <https://doi.org/10.1007/s00126-017-0762-4>

Large, R.R., 1977. Chemical evolution and zonation of massive sulfide deposits in volcanic terrains. *Econ. Geol.* 72, 549–572. <https://doi.org/10.2113/gsecongeo.72.4.549>

Leblanc, M., Billaud, P., 1982. Cobalt arsenide orebodies related to an upper Proterozoic ophiolite: Bou Azzer (Morocco). *Econ. Geol.* 77, 162–175. <https://doi.org/10.2113/gsecongeo.77.1.162>

Marques, A.F.A., Barriga, F.J.A.S., Chavagnac, V., Fouquet, Y., 2006. Mineralogy, geochemistry, and Nd isotope composition of the Rainbow hydrothermal field, Mid-Atlantic Ridge. *Miner. Depos.* 41, 52–67. <https://doi.org/10.1007/s00126-005-0040-8>

Marques, A.F.A., Barriga, F.J.A.S., Scott, S.D., 2007. Sulfide mineralization in an ultramafic-rock hosted seafloor hydrothermal system: From serpentinization to the formation of Cu – Zn – (Co) -rich massive sulfides. *Mar. Geol.* 245, 20–39. <https://doi.org/10.1016/j.margeo.2007.05.007>

Martin, A.J., Keith, M., Parvaz, D.B., McDonald, I., Boyce, A.J., McFall, K.A., Jenkin, G.R.T., Strauss, H., MacLeod, C.J., 2020. Effects of magmatic volatile influx in mafic VMS hydrothermal systems: Evidence from the Troodos ophiolite, Cyprus. *Chem. Geol.* 531, 119325. <https://doi.org/10.1016/j.chemgeo.2019.119325>

Martin, A.J., McDonald, I., MacLeod, C.J., Prichard, H.M., McFall, K., 2018. Extreme enrichment of selenium in the Apliki Cyprus-type VMS deposit, Troodos, Cyprus. *Mineral. Mag.* 82, 697–724. <https://doi.org/10.1180/mgm.2018.81>

Maslennikov, V. V., Maslennikova, S.P., Large, R.R., Danyushevsky, L. V., Herrington, R.J., Ayupova, N.P., Zaykov, V.V., Lein, A.Y., Melekestseva, I.Y., Tessalina, S.G., 2017. Chimneys in Paleozoic massive sulfide mounds of the Urals VMS deposits: Mineral and trace element comparison with modern black, grey, white and clear smokers. *Ore Geol. Rev.* 85, 64–106. <https://doi.org/10.1016/j.oregeorev.2016.09.012>

McCaig, A.M., Cliff, R.A., Escartín, J., Fallick, A.E., MacLeod, C.J., 2007. Oceanic detachment faults focus very large volumes of black smoker fluids. *Geology* 35, 935–938. <https://doi.org/10.1130/G23657A.1>

Melekestseva, I.Y., Maslennikov, V. V., Tret'yakov, G.A., Nimis, P., Beltenev, V.E., Rozhdestvenskaya, I.I., Maslennikova, S.P., Belogub, E. V., Danyushevsky, L., Large, R., Yuminov, A.M., Sadykov, S.A., 2017. Gold- and Silver-Rich Massive Sulfides from the Semenov-2 Hydrothermal Field, 13°31.13'N, Mid-Atlantic Ridge: A Case of Magmatic Contribution? *Econ. Geol.* 112, 741–773.

Müntener, O., Manatschal, G., Desmurs, L., Pettke, T., 2010. Plagioclase Peridotites in Ocean-Continent Transitions: Refertilized Mantle Domains Generated by Melt Stagnation in

the Shallow Mantle Lithosphere. *J. Petrol.* 51, 255–294.  
<https://doi.org/10.1093/petrology/egp087>

Nadoll, P., Angerer, T., Mauk, J.L., French, D., Walshe, J., 2014. The chemistry of hydrothermal magnetite: A review. *Ore Geol. Rev.* 61, 1–32.  
<https://doi.org/10.1016/j.oregeorev.2013.12.013>

Nimis, P., Zaykov, V. V., Omenetto, P., Melekestseva, I.Y., Tessalina, S.G., Orgeval, J.-J., 2008. Peculiarities of some mafic – ultramafic- and ultramafic-hosted massive sulfide deposits from the Main Uralian Fault Zone, southern Urals. *Ore Geol. Rev.* 33, 49–69.  
<https://doi.org/10.1016/j.oregeorev.2006.05.010>

Onuk, P., Melcher, F., Mertz-Kraus, R., Gäbler, M.-E., Goldmann, S., 2017. Development of a Matrix-Matched Sphalerite Reference Material (MUL-ZnS-1) for Calibration of In Situ Trace Element Measurements by Laser Ablation-Inductively Coupled Plasma-Mass Spectrometry. *Geostand. Geoanalytical Res.* 41, 263–272.  
<https://doi.org/10.1111/ggr.12154>

Paton, C., Hellstrom, J., Paul, B., Woodhead, J., Hergt, J., 2011. Iolite: Freeware for the visualisation and processing of mass spectrometric data. *J. Anal. At. Spectrom.* 26, 2508–2518. <https://doi.org/10.1039/C1JA10177B>

Patten, C.G.C., Pitcairn, I.K., Alt, J.C., Zack, T., Lahaye, Y., Teagle, D.A.H., Markdahl, K., 2020. Metal fluxes during magmatic degassing in the oceanic crust: sulfide mineralisation at ODP site 786P, Izu-Bonin forearc. *Miner. Depos.* 55, 469–489.  
<https://doi.org/10.1007/s00126-019-00900-9>

Patten, C.G.C., Pitcairn, I.K., Teagle, D.A.H., Harris, M., 2016. Sulphide mineral evolution and metal mobility during alteration of the oceanic crust: Insights from ODP Hole 1256D. *Geochim. Cosmochim. Acta* 193, 132–159. <https://doi.org/10.1016/j.gca.2016.08.009>

Peltonen, P., Kontinen, A., Huhma, H., Kuronen, U., 2008. Outokumpu revisited: New mineral deposit model for the mantle peridotite-associated Cu–Co–Zn–Ni–Ag–Au sulphide deposits. *Ore Geol. Rev.* 33, 559–617. <https://doi.org/10.1016/j.oregeorev.2007.07.002>

Perseil, E.A., Latouche, L., 1989. Découverte de microstructures de nodules polymétalliques dans les minéralisations manganésifères métamorphiques de Falotta et de Parsettens (Grisons-Suisse). *Miner. Depos.* 24, 111–116.

Pinto, V.H., Manatschal, G., Karpoff, A., Viana, A.R., 2015. Tracing mantle-reacted fluids in magma-poor rifted margins: The example of Alpine Tethyan rifted margins. *Geochemistry, Geophys. Geosystems* 16, 3271–3308.  
<https://doi.org/10.1002/2015GC005830>. Received

Reed, M.H., 1983. Seawater-basalt reaction and the origin of greenstones and related ore deposits. *Econ. Geol.* 78, 466–485.

Reed, M.H., Palandri, J., 2006. Sulfide Mineral Precipitation from Hydrothermal Fluids. *Rev. Mineral. Geochemistry* 61, 609–631. <https://doi.org/10.2138/rmg.2006.61.11>

Rona, P.A., 1985. Black smokers on the Mid-Atlantic Ridge. *Eos, Trans. Am. Geophys. Union* 66, 682–683. <https://doi.org/10.1029/EO066i040p00682-02>

Rouxel, O., Fouquet, Y., Ludden, J.N., 2004a. Copper Isotope Systematics of the Lucky Strike, Rainbow, and Logatchev Sea-Floor Hydrothermal Fields on the Mid-Atlantic Ridge. *Econ. Geol.* 99, 585–600.

Rouxel, O., Fouquet, Y., Ludden, J.N., 2004b. Subsurface processes at the lucky strike hydrothermal field, Mid-Atlantic ridge: Evidence from sulfur, selenium, and iron isotopes. *Geochim. Cosmochim. Acta.* <https://doi.org/10.1016/j.gca.2004.11.029>

Schaltegger, U., Desmurs, L., Manatschal, G., Müntener, O., Meier, M., Frank, M., Bernoulli, D., 2002. The transition from rifting to sea-floor spreading within a magma-poor rifted margin: field and isotopic constraints. *Terra Nova*. 14, 156–162.

Sohrin, Y., Iwamoto, S.I., Akiyama, S., Fujita, T., Kugii, T., Obata, H., Nakayama, E., Goda, S., Fujishima, Y., Hasegawa, H., Ueda, K., Matsui, M., 1998. Determination of trace elements in seawater by fluorinated metal alkoxide glass-immobilized 8-hydroxyquinoline concentration and high-resolution inductively coupled plasma mass spectrometry detection. *Anal. Chim. Acta* 363, 11–19. [https://doi.org/10.1016/S0003-2670\(98\)00074-9](https://doi.org/10.1016/S0003-2670(98)00074-9)

Song, X.-Y., Zhou, M. F., Cao, Z.-M., Sun, M., Wang, Y.-L., 2003. Ni–Cu–(PGE) magmatic sulfide deposits in the Yangliuping area, Permian Emeishan igneous province, SW China. *Miner. Depos.* 38, 831–843. <https://doi.org/10.1007/s00126-003-0362-3>

Talhammer, O., Stumpfl, E.F., Panayiotou, A., 1986. Postmagmatic, hydrothermal origin of sulfide and arsenide mineralizations at Limassol Forest, Cyprus. *Miner. Depos.* 21, 95–105.

Tao, C., Lin, J., Guo, S., Chen, Y.J., Wu, G., Han, X., Christopher, R., Yoerger, D.R., Zhou, N., Li, H., Su, X., Zhu, J., Legs, D.-, Tao, C., Lin, J., Guo, S., Chen, Y.J., Wu, G., Han, X., German, C.R., Yoerger, D.R., Zhou, N., Li, H., Su, X., Zhu, J., DY115-19 and DY115-20 Science Parties, 2012. First active hydrothermal vents on an ultraslow-spreading center: Southwest Indian Ridge. *Geology* 40, 47–50. <https://doi.org/10.1130/G32389.1>

Tivey, M.K., 2007. Generation of Seafloor Hydrothermal Vent Fluids and Associated Mineral Deposits. *Oceanography* 20, 50–65.

Toffolo, L., Nimis, P., Martin, S., Tumiati, S., Bach, W., 2017. The Cogne magnetite deposit (Western Alps, Italy): A Late Jurassic seafloor ultramafic-hosted hydrothermal system? *Ore Geol. Rev.* 83, 103–126. <https://doi.org/10.1016/j.oregeorev.2016.11.030>

Webber, A.P., Roberts, S., Murton, B.J., Mills, R.A., Hodgkinson, M.R.S., 2017. The formation of gold-rich seafloor sulfide deposits: Evidence from the Beebe hydrothermal vent field, Cayman Trough. *Geochemistry, Geophys. Geosystems* 18, 2011–2027. <https://doi.org/10.1002/2017GC006922>.

Wilson, S.A., Ridley, W.I., Koenig, A.E., 2002. Development of sulfide calibration standards for the laser ablation inductively-coupled plasma mass spectrometry technique. *J. Anal. At. Spectrom.* 17, 406–409. <https://doi.org/10.1039/B108137H>

Wohlgemuth-Ueberwasser, C.C., Viljoen, F., Petersen, S., Vorster, C., 2015. Distribution and solubility limits of trace elements in hydrothermal black smoker sulfides: An in-situ LA-ICP-MS study. *Geochim. Cosmochim. Acta.* <https://doi.org/10.1016/j.gca.2015.03.020>

Xiong, Y., 2003. Predicted equilibrium constants for solid and aqueous selenium species to 300 °C: Applications to selenium-rich mineral deposits. *Ore Geol. Rev.* 23, 259–276. [https://doi.org/10.1016/S0169-1368\(03\)00038-6](https://doi.org/10.1016/S0169-1368(03)00038-6)

Yuan, B., Yang, Y., Yu, H., Zhao, Y., Ding, Q., Yang, J., Tang, X., 2018. Geochemistry of pyrite and chalcopyrite from an active black smoker in 49.6°E Southwest Indian Ridge. *Mar. Geophys. Res.* 53, 441–461. <https://doi.org/10.1007/s11001-017-9324-5>

Zierenberg, R.A., Koski, R.A., Morton, L., Bouse, R.M., Shanks, W.C., 1993. Genesis of massive sulfides deposits on a sediment-covered spreading center, Escabana Trough, Southern Gorda Ridge. *Econ. Geol.* 88, 2069–2098.

**Declaration of interests**

The authors declare that they have no known competing financial interests or personal relationships that could have appeared to influence the work reported in this paper.

The authors declare the following financial interests/personal relationships which may be considered as potential competing interests:

Journal Pre-proof